Ultramicroscopy 251 (2023) 113753

Contents lists available at ScienceDirect

Ultramicroscopy

journal homepage: www.elsevier.com/locate/ultramic

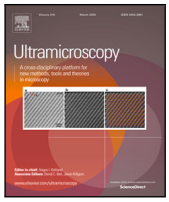

Neutral helium atom microscopy

Adrià Salvador Palau [a], Sabrina Daniela Eder [a], Gianangelo Bracco [b], Bodil Holst [a,*]

[a] Department of Physics and Technology, University of Bergen, Allegaten 55, Bergen, 5007, Norway
[b] CNR-IMEM, Department of Physics, University of Genova, via Dodecaneso 33, Genova, 16146, Italy

ARTICLE INFO

Keywords:
Microscopy
SHeM
Molecular beams
Helium atom scattering
Neutral helium microscopy
NAM
Neutral atom microscopy

ABSTRACT

Neutral helium atom microscopy, also referred to as scanning helium microscopy and commonly abbreviated SHeM or NAM (neutral atom microscopy), is a novel imaging technique that uses a beam of neutral helium atoms as an imaging probe. The technique offers a number of advantages such as the very low energy of the incident probing atoms (less than 0.1 eV), unsurpassed surface sensitivity (no penetration into the sample bulk), a charge neutral, inert probe and a high depth of field. This opens up for a range of interesting applications such as: imaging of fragile and/or non-conducting samples without damage, inspection of 2D materials and nano-coatings, with the possibility to test properties such as grain boundaries or roughness on the Ångström scale (the wavelength of the incident helium atoms) and imaging of samples with high aspect ratios, with the potential to obtain true to scale height information of 3D surface topography with nanometer resolution: nano stereo microscopy. However, for a full exploitation of the technique, a range of experimental and theoretical issues still needs to be resolved. In this paper we review the research in the field. We do this by following the trajectory of the helium atoms step by step through the microscope: from the initial acceleration in the supersonic expansion used to generate the probing beam over the atom optical elements used to shape the beam (resolution limits), followed by interaction of the helium atoms with the sample (contrast properties) to the final detection and post-processing. We also review recent advances in scanning helium microscope design including a discussion of imaging with other atoms and molecules than helium.

1. Introduction

Neutral helium atom microscopes are surface characterisation tools that apply a beam of neutral helium atoms as imaging probe. The instruments exploit a supersonic expansion of helium gas from a high pressure reservoir (100 bar range) through a nozzle into vacuum to generate a high-intensity beam with a narrow velocity distribution, which is then collimated or focused onto a sample. The scattered intensity signal is recorded "point by point" and used to create an image of the sample in a manner similar to other beam probe microscopy techniques such as scanning electron microscopy or helium ion microscopy, but with the crucial difference that due to the very low energy[1] and strict surface sensitivity of the neutral helium beam, the neutral helium atoms scatter off the outermost electron density distribution of the sample. There is no penetration into the sample-material and no photons or secondary electrons are generated during the scattering process.

Several abbreviations have been used for neutral helium microscopy over the years, i.e. NEMI for NEutral MIcroscope [1], HeM for Helium Microscope and NAM for Neutral Atom Microscopy [2], however the community now seems to have agreed on SHeM for Scanning Helium Microscope, which was actually also one of the first abbreviations, introduced by MacLaren and Allison already in 2004 [3]. We will use the abbreviation SHeM for the rest of this paper.

The research behind neutral helium microscopes includes four main areas, which can be mapped to the different stages of the imaging probe trajectory. Firstly modelling of the supersonic expansion of helium gas into vacuum, needed to establish the intensity and matter wave properties of the probing helium beam. Secondly, de-Broglie matter wave optics, which describes the interaction of the neutral helium atoms with the optical elements, such as zone plates, pinholes and mirrors, critical for the microscope resolution. Thirdly, helium atom surface scattering, modelling the interaction between the neutral helium atoms and the sample, thus determining the contrast properties. Finally the helium atom detection, targeting the difficult problem of detecting hard-to-ionise neutral helium atoms. In addition to these four area

* Corresponding author.
E-mail address: bodil.holst@uib.no (B. Holst).

[1] The energy of the helium atoms is determined by the temperature of the nozzle which can be cooled or heated. The energy range is typically between 20 meV corresponding to a de-Broglie wavelength of around 0.1 nm, and 60 meV (room temperature beam) corresponding to a wavelength of around 0.05 nm, see Eq. (3) Helium atoms with energies in this range are referred to as thermal helium atoms, a term which is also used in this paper.

https://doi.org/10.1016/j.ultramic.2023.113753
Received 8 July 2022; Received in revised form 20 April 2023; Accepted 4 May 2023
Available online 10 May 2023
0304-3991/© 2023 The Author(s). Published by Elsevier B.V. This is an open access article under the CC BY license (http://creativecommons.org/licenses/by/4.0/).

comes research specifically dedicated to the application of scanning helium microscopes. This includes problems such as optimisation of the overall configuration of the tool, advanced imaging techniques (including stereo-imaging), signal processing and image analysis.

For this review we have provided an open-source implementation of the solution to the Boltzmann equation in spherical coordinates used in previous helium microscope simulation work. It is meant as a service for those interested in pursuing their own helium microscope designs. The code can be found on GitHub: [4]. We would also like to draw attention to the ray tracing simulation program of the Cambridge SHeM, provided by Lambrick and Seremet, also available on GitHuB [5].

We begin this review with a brief historical overview of the research that made neutral helium microscopy possible. Then we follow the trajectory of a helium atom through a neutral helium microscope as described above. In this way, we review the background research, step by step. Then we move on to discuss the latest research on microscope design and imaging techniques and we present an overview of the SHeM images published up till now. The paper finishes with an outlook on the expected future of the field.

1.1. Background

In 1930 Estermann and Stern scattered an effusive beam of neutral helium atoms off LiF(100) and saw diffraction peaks [6]. Their groundbreaking work had been made possible thanks to previous work by Dunnoyer who established the first directed atom beam in 1911 [7].

It took another twenty years for Kantrowitz and Grey to devise a helium source with a narrower velocity distribution [8]. This was achieved thanks to a supersonic expansion of helium gas into a lower-pressure chamber (see Section 2.1). Notwithstanding the clear improvement that this brought, much narrower velocity distributions and higher intensities were imperative for the success of neutral helium atoms as a scattering probe.

Such beam properties were achieved in the early 1970s thanks to the improvement of vacuum techniques and the introduction of small nozzles, which allowed for supersonic expansion into ultra high vacuum. The central part of the beam was selected using a conically shaped aperture, a so called skimmer — until that point, slits had been preferred. By the 1980s, nozzle technology had advanced so much that the velocity distribution of the helium beams had become narrow enough that the small energy changes[2] resulting from the creation or annihilation of surface phonons could be measured [9]. This propelled helium atom scattering as a method suitable to study surface dynamics [10–13].

Eventually, physicists began to speculate on how the surface sensitivity of helium could also be used to construct an imaging instrument. It soon became clear that focusing optics was a particular challenge. Neutral, ground-state helium has the smallest polarisability of all atoms and molecules. Hence manipulation via electrostatic or magnetic fields is essentially not possible unless one uses ^{3}He, which is in principle possible, but up till now ^{3}He has not been applied in microscopy experiments. Furthermore, helium atoms at thermal energies do not penetrate solid materials. In practice, the only possible way to manipulate them is via their de-Broglie matter-wave properties. This leaves only three possibilities: simple collimation, focusing via mirror reflection or focusing via diffraction from free-standing structures (zone plates).

To the best of our knowledge, the idea of a neutral helium microscope was mentioned for the first time in an official scientific context in 1990 when Doak presented results demonstrating focusing in 1D by reflecting a neutral, ground state helium beam off a mechanically bent, gold-coated piece of mica at two conferences [14,15], see also [16,17]. In 1991 Carnal et al. presented the first experiment on 2D focusing of neutral helium beams: The focusing of a beam of metastable helium atoms using a Fresnel zone plate [18]. In 1997 Holst and Allison achieved astigmatic focusing in 2D by scattering a neutral, ground state helium beam off a Si(111)-H(1 × 1) surface electrostatically bent to a parabolic shape [19,20]. The silicon wafer used had a thickness of 50 μm. The area of least confusion had a spot diameter of 210 μm, which Holst et al. used in a later experiment to image the ionisation region of an electron bombardment detector [21]. In 1999 Grisenti et al. obtained the first focusing of neutral, ground state helium with a zone plate. They used a micro skimmer as a source and achieved a focused spot diameter of less than 2 μm [22].

In 1999 it was proposed that by changing the boundary conditions from round to ellipsoidal a mirror without stigmatic error could be obtained by electrostatic bending [23], see also [24–26]. In 2010 Fladischer et al. achieved near stigmatic focusing of helium atoms using this method [27]. Despite work on the optimisation of the hydrogen passivation of the Si(111) surface [28] and the development of a transport procedure that allowed transport of mirrors to microscope systems [29], it remained a problem with the Si(111)-H(1 × 1) mirrors that there is a considerable loss in intensity in the specular beam due to diffraction from the corrugated electron density distribution at the surface [30–32]. In 2008 Barredo et al. showed that the reflectivity of an atom mirror could be dramatically improved by coating the silicon wafer surface with a 1–2 nm layer of lead [33]. This so called-quantum stabilised mirror demonstrated a specular helium reflectivity of 67%. In a later work Anemone et al. explored the use of flexible thin metal crystals as focusing mirrors [34], following an early attempt from 1999 [26]. Despite the promising achievements in bent mirror focusing, the problem remains that to achieve focal spots at the nanometer range, near uniformly flat crystals without bow and warp are necessary. Work has been done on thin wafer characterisation targeted for atom mirror applications [35–40], on the improvement of the quality (flatness of a free, un-clamped wafer) of ultra-thin Si wafers for mirror applications [41] and on how wafer imperfections identified through this characterisation can be compensated for by a multiple electrode structure for bending [42], but even so the very high technological requirements needed for nanometer range focusing, seems to have put an end to research on the creation of focusing atom mirrors through thin crystal bending, at least for the time being.

A very different approach for making atom focusing mirrors was presented by Schewe et al. in 2009 [43]. 1D focussing of a helium beam down to 1.8 μm was demonstrated by quantum reflection from a cylindrical, concave quartz mirror. For a sufficiently small normal component of the incident wave vector of the atom, quantum reflection at the attractive branch of the helium-surface interaction potential is achieved. The great advantage of this technique is 100% reflectivity into the focus from a surface that can be microscopically rough [44], so that producing the mirror suddenly becomes very easy - a simple, commercial glass substrate, machined into a suitable elliposoidal shape, can be used. The problem is that near-grazing incidence is required to make the wave vector component small enough, and this puts a limit to how large a beam that can be used.

An alternative path for making atom focusing mirrors without thin crystal bending was proposed in 2011 by Sutter et al. who showed that a high-reflecting mirror with a specular helium reflectivity of 23% could be obtained with a graphene-terminated Ru(0001) thin film grown on c–axis sapphire [45]. Earlier work had shown that monolayer graphene can grow on polycrystalline Ru thin films on arbitrarily shaped surfaces [46], this in principle, paves the way for making a focusing mirror by growing a thin layer of ruthenium on a sapphire substrate polished to the desired mirror shape and terminate it with graphene. Work pursing this is ongoing [47].

Despite the various promising approaches, no functioning SHeM based on mirror focusing has been built so far. The first SHeM image

[2] meV range.

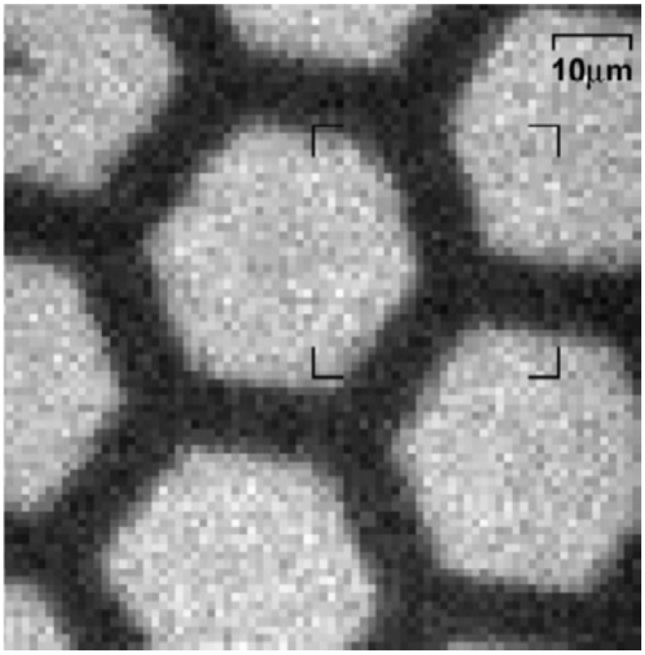

Fig. 1. First SHeM image. The image is a 2D shadow image, showing a free standing grating structure. The image is obtained by scanning the focused beam across the sample, recording the signal from the transmitted helium atoms, see Fig. 2.
Source: Image reproduced from [48].

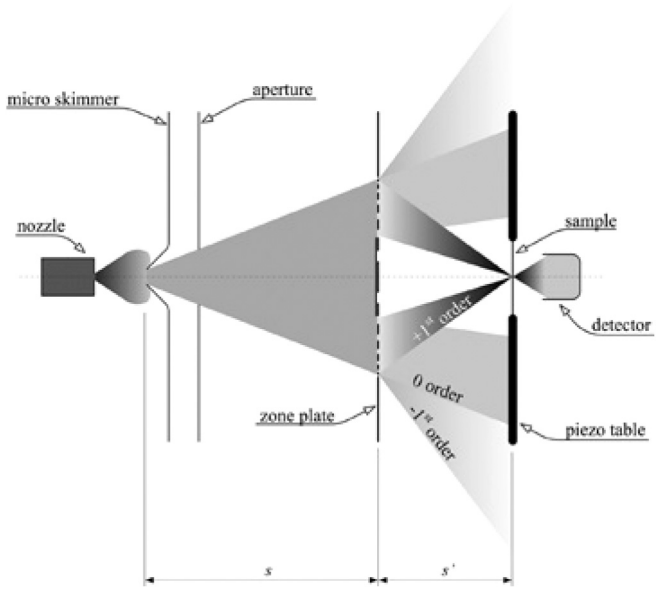

Fig. 2. Diagram of the first SHeM microscope used to obtain the image shown in Fig. 1. The beam is generated by a free-jet (supersonic) expansion through a micro-skimmer (see Section 6.1) which is imaged onto the sample plane by the zone plate's plus first diffraction order. In addition, the zero as well as the minus first order are indicated. s is the source to zone plate distance and s' the distance from zone plate to image plane. The indicated aperture just serves to filter background from the source. The sample is scanned across the beam by a piezo table. The transmitted intensity of the beam is recorded at the back to obtain an image in transmission mode. This first SHeM microscope did not have an order-sorting aperture [50].
Source: Figure reproduced from [48].

was obtained by Koch et al. in 2008 [48], see Fig. 1.[3] Koch et al. obtained a 2D shadow image of a free standing grating structure with a resolution of around 2 μm using a micro-skimmer (see Section 6.1) and a Fresnel zone plate to focus the helium beam onto the grating. A diagram of the instrument can be seen in Fig. 2. The best SHeM resolution obtained with a zone plate up till now is slightly less than 1 μm, demonstrated by Eder et al. [49]. This is very far from the theoretical resolution limits which are discussed in Section 3. Note that for the zone plate microscope configuration, the 0-order component of the beam should be blocked from entering the sample chamber in order to minimise the background signal. This can be done using a so called order-sorting aperture, also known from X-ray optics. An order sorting aperture for helium focusing with a zone plate was demonstrated in [50]. In 2008 a zone plate was also used by Reisinger et al. to focus a beam of Deuterium molecules, as a first demonstration of the potential of making microscopes with other atomic and molecular beams [51], see also [52]. For a description of the zone plates used for neutral helium microscopy see [53–56].

After the work of Koch et al. other research groups focused on a simpler configuration: the pinhole microscope. This configuration uses a small circular aperture (a pinhole) to collimate the beam instead of focusing optics. The resolution is determined by the size of the pinhole, see Fig. 4. Using a configuration with a pinhole placed directly in front of the nozzle, Witham and Sánchez managed to obtain the first SHeM images in reflection mode in 2011 [2], see Fig. 3. The initial resolution was 1.5 μm and later 0.315 μm [57], which remains the highest resolution obtained so far with a neutral helium atom microscope. In 2014 Witham and Sánchez also demonstrated reflection imaging with a Krypton beam [58], see also [59].

Around the same time as Witham and Sánchez other researchers had started working on pinhole microscopes with a different design, using a skimmer in combination with a collimating pinhole aperture [60]. Their approach was inspired by a set of unpublished reports on neutral helium atom microscopy, written by Lower around 1992 [61]. In connection with this review these reports have now been made publicly available for the first time [62–65]. The idea of a pinhole microscope is also discussed in [66]. In the reports Lower discusses helium microscopy based on focusing with mirrors and zoneplates and he also introduces the idea of a microscope based purely on collimation which he calls a pinhole microscope.

The first images from a pinhole microscope of the type originally proposed by Lower were published in 2014 [67]. For a diagram of the setup, see Fig. 5. The advantage of using a skimmer is that the perturbation of the helium atoms trajectories through backscattering is reduced, see for example [68] and Section 2.2.3. This means that a pinhole microscope with a skimmer should in principle have an increased intensity in the beam spot on the sample and provide a narrow, well defined velocity distribution. The latter is of particular interest for contrast properties, see Section 4. A counter argument in favour of the Witham–Sánchez design is that here the pinhole can be brought closer to the nozzle, which in principle should also increase the intensity for a given working distance (distance between pinhole and sample). No detailed performance comparisons between the two designs have been presented in the literature up till now. At present it seems that the community mainly pursues the second design, where a skimmer is used. This including the most recent instrument by Bhardwaj et al. [69].

2. The helium source

A typical SHeM source follows the design established for helium atom scattering (HAS) [60,67,70]: helium is accelerated in a supersonic

[3] For the first SHeM microscopy images Koch et al. used an instrument popularly known as MAGIE [48]. MAGIE was designed for this purpose by Graham, Holst, Toennies and technical staff at the Max Planck Institute for Fluid Mechanics in Göttingen. The instrument was built in the institute workshop. Ernst purchased MAGIE from the Max Planck Society following the retirement of Toennies and so the experiments of Koch et al. were carried out at TU-Graz.

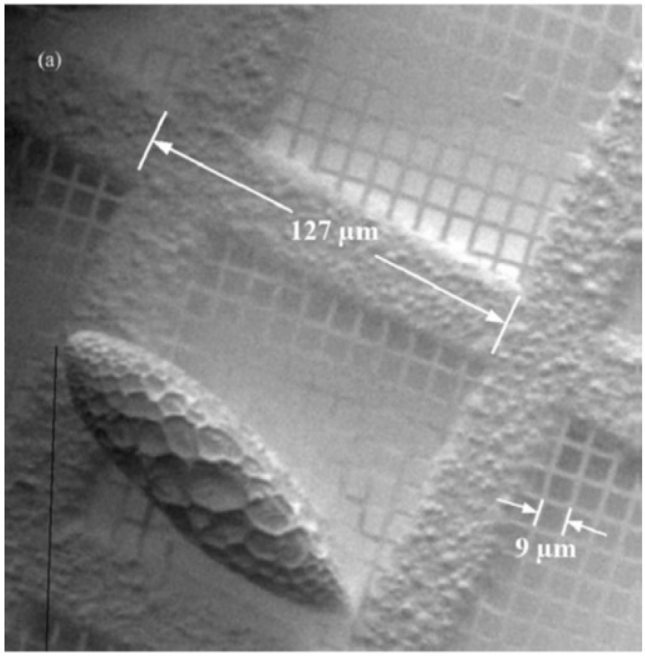

Fig. 3. First SHeM image obtained in reflection mode. The image shows an uncoated pollen grain on a Quantifoil grid. The image is created by detecting the atoms scattered over a particular range of angles.
Source: Image reproduced from [2].

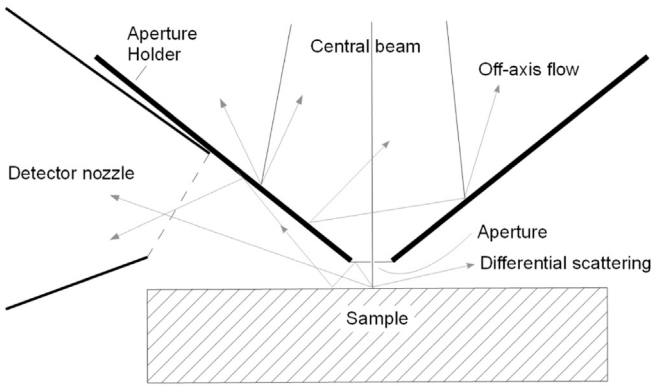

Fig. 4. Diagram of the first pinhole SHeM.
Source: Figure reproduced from [2].

expansion from a high pressure reservoir, through a nozzle, into a vacuum chamber, known as the expansion chamber [71]. There, the central part of the beam is selected by a conically shaped aperture, called the skimmer.[4]

When designing a Helium Source, one can essentially choose five parameters: temperature, pressure, nozzle radius,[5] skimmer diameter and distance between skimmer and nozzle.[6] In general, small nozzles and high pressures produce brighter[7] sources and therefore are more efficient in reducing undesired effects such as back-scattering interference (for a given flow, the beam is more directed) [73,74]. It should be noted though that pulsed sources with larger nozzles have also been pursued as a mean to create high intensity supersonic beams with high parallel speed ratio [75].[8] An approach for achieving beam brightening through shock-wave suppression can be found in [76]. Cold sources are more intense than warm sources and produce higher parallel speed ratios [68,70], which allows them to reach higher centreline intensities. The absolute differences between a cold (liquid nitrogen cooled) and a warm source at the same pressure can easily be on the order of $1 \cdot 10^{13}$counts/s m^2 at a distance of 2.44 m, which approximates to a 40% difference [68] (see Fig. 6).

Once the nozzle size and temperature have been chosen, obtaining the beam properties amounts to (1) solving the supersonic expansion of the Helium gas into vacuum, and (2) calculating the beam intensity after the initial expansion. This chapter is structured with these two steps in mind: first, we discuss the work done on describing the supersonic expansion, and then we discuss the different models that give the beam intensity downstream.

2.1. The supersonic or free-jet expansion

The theory describing supersonic expansions, also sometimes referred to as free jet expansions, was developed in the 1970s and 1980s, and is based on splitting the expansion into two regimes: the first regime, within the nozzle, follows a Navier–Stokes flow, and is solved through the isentropic nozzle model [7,77]. The second regime, from the nozzle exit onward, is modelled through the Boltzmann equation. The flow is obtained either by solving the corresponding integrals under simplifying assumptions [78,79] or using Direct Simulation Monte Carlo (DSMC) [80–82].

2.1.1. The isentropic nozzle model

Within the nozzle, the helium gas density is high (typically up to 200 bar) and the flow is modelled with Navier Stokes equations. The isentropic nozzle model gives the total flux per unit time (from now on, centre line intensity) stemming from a de Laval nozzle[9] (assuming that the nozzle is cut-off in the sonic plane). This derivation considers an ideal gas in which the flow can be assumed to be a reversible and adiabatic process. Therefore the gas can be considered isentropic — which means that the following analytical equation of the intensity can be obtained [7].

$$I_0 = \frac{P_0}{k_B T_0}\sqrt{\frac{2k_B T_0}{m}}\left(\pi r_{nz}^2\right)\sqrt{\frac{\gamma}{\gamma+1}}\left(\frac{2}{\gamma+1}\right)^{1/(\gamma-1)}, \tag{1}$$

where T_0, P_0 are the temperature and the pressure in the source. r_{nz} is the radius of the nozzle and m is the mass of a helium atom. γ is the heat capacity ratio ($\gamma = 5/3$ for helium), and k_B is the Boltzmann constant. Along a streamline, the adiabatic condition also leads to the conservation of enthalpy per unit mass [77]

$$h_0 = h + \frac{1}{2}v(x)^2 \tag{2}$$

where h_0 is the enthalpy of the gas in the source where the gas is at rest, while $h(x)$ is the enthalpy at distance x from the source during the expansion where the gas is moving with velocity $v(x)$ and the last term is the kinetic energy per unit mass. For a perfect monoatomic gas $h(x) = \frac{5}{2}k_B T(x)$ and during the expansion we expect a cooling of the gas and far from the source $T_0 \gg T(x)$, therefore $h(x)$ can be neglected with respect to h_0 and practically all the enthalpy in

[4] The Witham–Sánchez pinhole microscope design skip the skimmer altogether and use a single collimating aperture downstream [2].

[5] The issue of nozzle design is left as outside of the scope of this paper. For a discussion of this topic see for example [71,72].

[6] There are also important considerations that needs to be done regarding vacuum chamber geometry, required pumping speed, shape of the skimmer etc., but that is beyond the scope of this paper.

[7] Count rate per steradian and unit area of the source.

[8] The speed ratio of a supersonic molecular beam is defined as $\frac{\bar{v}}{\Delta v}$ where $\bar{v}$ is the most probable velocity and Δv is the Full Width at Half Maximum of the velocity distribution.

[9] de Laval refers to the nozzle profile. In practice most groups simply use a small hole (typically a commercial electron microscope aperture).

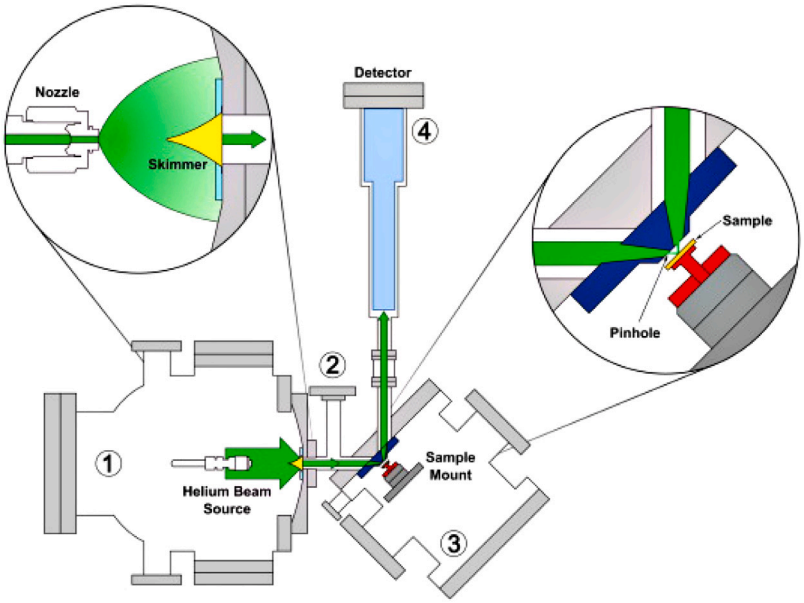

Fig. 5. Schematic diagram of the second pinhole SHeM using a skimmer in combination with a pinhole. The helium beam is generated in a free-jet (supersonic) expansion in the source chamber (1), passing through a differential pumping stage (2) to the pinhole optics. The collimated beam hits the sample in the sample chamber (3). The scattered helium entering the detector chamber (4) where it stagnates to form a stable pressure, which is measured. The image is produced by scanning the sample under the beam.
Source: Figure reproduced from [67].

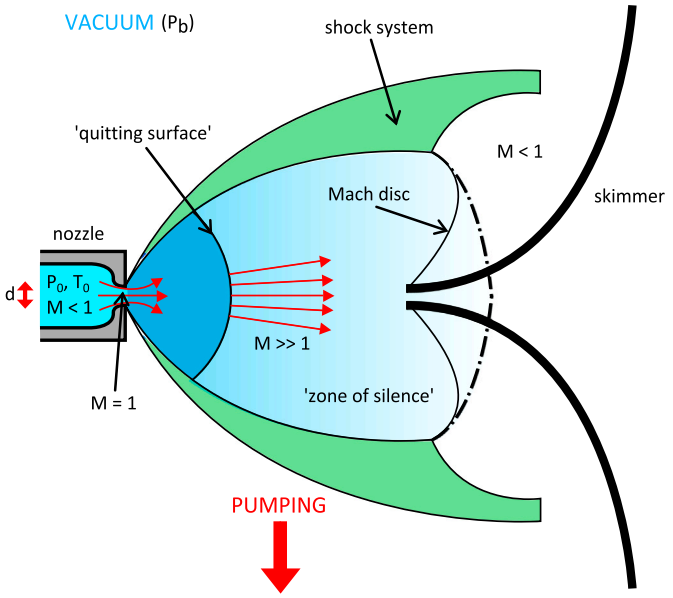

Fig. 6. Schematic diagram of a free-jet (supersonic) expansion. The source expands from a helium reservoir with pressure P_0 and temperature T_0 through a nozzle of diameter d into a vacuum. The Mach number M (ratio of flow velocity to the local speed of sound) rapidly increases during the initial expansion. As the expansion continues there is a transition from continuum flow to molecular flow, which is often modelled with the so-called "quitting surface" (see Fig. 7). The central part of the beam is sampled by a skimmer. In modern, high-efficient pumping systems the position of the Mach disc is often behind the skimmer and for low background pressure the shock structure and Mach disc are less pronounced and disappear.
Source: Figure reproduced from [60].

the source is transformed into kinetic energy. From Eq. (2) one can obtain the terminal velocity, $\bar{v}$, which can be used to provide the most probable de-Broglie wavelength of the atoms in the beam: [7]:

$$\bar{v} = \sqrt{\frac{5k_B T_0}{m}}. \tag{3}$$

This model is used to calculate the total flow from the nozzle — as it is well known that helium is the closest we get to an ideal gas [83]. Some groups also choose to add a correction given by the thickness of the boundary layer in a real gas. Beijerinck and Verster provide a correction factor for a monoatomic gas [71]. To our knowledge, all helium microscopy papers modelling the intensity of the helium beam use an initial intensity derived from the isentropic nozzle model (see Section 2.2.2 for a breakdown).

Finally since results for beams which are mixtures of two different gases will be also presented in Section 6, the generalisation of Eq. (3) for a mixture of monoatomic gases is [77]

$$\bar{v} = \sqrt{\frac{5k_B T_0}{m_{av}}} \tag{4}$$

where $m_{av} = f_1 m_1 + f_2 m_2$ is the weighted average mass with f_i the mass fraction in the mixture of component i having mass m_i, this equation shows that both gas components have a common velocity, albeit a velocity difference, the velocity slip, is generally present. Further comments will be given when results on mixtures will be discussed.

2.1.2. Post-nozzle flow

Once the helium atoms have left the nozzle, the pressure drops and the flow is governed by the Boltzmann equation — as the Navier Stokes equations cease to apply. There are two main methods to solve the flow: either by numerically solving the Boltzmann equation under stringent assumptions [7,84,85] or by simulating the particle flow using DSMC. The latter method is more computationally intensive, but also more accurate than the former as it relies on fewer assumptions: For the first method, one typically assumes that the nozzle is a point source [78]. This assumption is grounded on work from Sherman and Ashkenas, which showed that a few nozzle diameters downstream, free jet streamlines become straight and can be extrapolated to a single point of origin close to the nozzle [84,85]. The flow then can be solved using the collision integral for particles following Bose–Einstein statistics. The isentropic nozzle model at a short distance from the nozzle is used

to obtain the initial conditions to start the integration.[10] To solve this equation, a velocity distribution, and an interaction potential have to be assumed. The equations needed to solve the expansion are included in [7,68]. As mentioned above for this review, we provide an open-source implementation of the solution to the Boltzmann equation in spherical coordinates [4].

The velocity distribution of the atoms is taken to be an ellipsoidal Maxwellian:

$$f_{\mathrm{ell}}\left(\vec{v}\right) = n\left(\frac{m}{2\pi k_{\mathrm{B}} T_{||}}\right)^{\frac{1}{2}}\left(\frac{m}{2\pi k_{\mathrm{B}} T_{\perp}}\right)\cdot \exp\left(-\frac{m}{2k_{\mathrm{B}} T_{||}}(v_{||}-\bar{v})^2 - \frac{m}{2k_{\mathrm{B}} T_{\perp}} v_{\perp}^2\right). \tag{5}$$

The choice of an ellipsoidal Maxwellian velocity distribution forms the basis to solve the spherically symmetrical Boltzmann equation [86]. In these models, the expansion's macroscopic properties are expressed in a spherical coordinate system. The temperature is split in two terms, modelling the velocity distributions of the radial and angular component of the velocity in spherical coordinates $v_{\parallel}$ and $v_{\perp}$: $T_{||}$ and $T_{\perp}$. These are proportional to the variance of the velocity in that coordinate system, for example $T_{||} = \frac{m}{k_{\mathrm{B}}}\langle(v_{||}-v_{||}^0)^2\rangle$, where $v_{||}^0$ is the parallel component of the mean velocity vector, $\bar{v}$ is the most probable velocity of the beam along the radial direction and n is the number density of atoms.

On top of the assumption regarding the velocity distribution of the atoms, an interaction potential must be assumed. There are several options for this potential: the Lennard-Jones potential [87], the Tang, Toennies and Yu (TTY), and the Hurly Moldover (HM) potentials [88,89] being amongst the best known. Results of previous calculations show that the Lennard-Jones potential is accurate for source temperatures as low as 80 K [90,91]. Therefore, this is often the preferred choice by practitioners in the field as the Helium source is rarely cooled below this temperature [90–92]. A detailed description of the Lennard-Jones potential and its implementation in the Boltzmann equation can be found in [92].

The numerical solution of the Boltzmann equation in its spherical approximation provides the evolution of the average gas velocity, and the temperatures $T_{||}$ and $T_{\perp}$ with respect to the distance from the nozzle. This solution can then be used to determine the intensity of the beam at the sample plane by means of the so called quitting surface model — see Section 2.2.1. This solution can also be used to obtain the velocity distribution and speed ratio of the beam. These have been shown to be in good agreement with experimental data [70].

As mentioned above an alternative way of solving the Boltzmann equation, requiring less assumptions, is to directly simulate particle-to-particle interactions using DSMC [80,81]. This method addresses the numerical infeasibility of simulating the flow particle by grouping those particles onto pseudo-molecules that are taken to represent a larger group of real molecules. DSMC requires assumptions on the interaction of the pseudo-molecules with different materials and with each other. These are normally phenomenological models such as the hard sphere model [80], the variable hard sphere model [93] and others [94]. DSMC is truer to nature than solving the Boltzmann equation under stringent assumptions but is also much more computationally expensive. Several papers have used this method to understand the behaviour of the helium expansion [82,95,96].

2.2. Intensity after the initial expansion

As the helium atom travels further away from the nozzle, it interacts less and less with neighbouring atoms. This means that modelling the supersonic expansion all the way to the sample plane is numerically inefficient.

Therefore, theorists often choose to use the fact that the Knudsen number of the flow increases with distance to the source, and that quasi-molecular flow is often reached before the first optical element, usually the skimmer, to build simplified models of the intensity. Quasi-molecular flow allows for the recovery of analytical expressions of the centre-line intensity, as particles can be assumed to travel in a straight line without further interactions.

Over the years, several intensity models have been proposed for helium sources. A combination of arbitrary variable labelling, numerical simplifications and empirical formulae has left researchers with no unified intensity models. Here we present the different intensity models and explain how they compare with each other.

The skimmer is placed at a distance x_S from the nozzle. Take a as the distance between the skimmer and the axial point in which the intensity is measured. The distance between the nozzle and the measuring point is then $(x_S + a)$. All the rest of physical variables correspond to those presented in Section 2.2.1.

We propose that the intensity should always be given as particles per second per unit area.[11] The analytical formulae for intensity found in literature can be divided into two categories:

Firstly, the modified symmetrical flux models which falls into two types: (i) those that treat the nozzle as a source of a spherically symmetrical flux, and account any excess intensity by using an empirical factor [71], (ii) those that on top of this consider the thermal properties of the supersonic expansion through a dependency on the beam's speed ratio. Secondly the quitting surface intensity models which are (iii) those that explicitly integrate the quitting surface.[12] Both categories of intensity models are limited in that they rely on overly simplistic assumptions, but they are useful in that they provide analytical expressions for the intensity. We start in the next section by considering the second category.

2.2.1. The quitting surface intensity models

Some of the most popular intensity models relies on the quitting surface model [68,78,97] with the associated definition "virtual source". A quitting surface[13] is a useful theoretical construct which assumes that at a given point in the beam's supersonic expansion, particles start travelling in straight lines. This point is defined through asymptotic conditions on the properties of the expansion; either as the point in which the Mach number[14] of the expansion approaches its predicted terminal Mach number [2,99] or as the point in which the parallel and perpendicular temperature of the Maxwellian distribution used to model the expansion decouple [100].

The main utility of this model is that the intensity and velocity distribution of the beam can be obtained by integrating this spherical particle-emitting surface. This distribution can then be backtraced from the quitting surface to a so called virtual source plane, which describes the intensity and velocity distribution that a source would need to have to give rise to the observed distribution at the quitting surface. The virtual source plane is taken as the plane where the spatial distribution has the minimum extension. This means that the virtual source can be seen as the object that, with a view reduced by the skimmer, is imaged onto the sample plane by the zone plate in the zone plate microscope. Zone plates have actually been used in combination with large skimmers to obtain direct images of the supersonic expansion [52,92,101]. The difficulty associated with this method is the relative arbitrarity of

[10] This is a rather arbitrary distance that must be large enough to guarantee spherical symmetry and small enough to satisfy equilibrium conditions, typically a few nozzle diameters.

[11] We chose unit area over steradians to signify the departure from spherical symmetry typical of supersonic beams.

[12] Or an equivalent concept — known as the virtual source [73]

[13] Also referred to as "last collision surface" [71,98].

[14] Ratio of flow velocity to the local speed of sound, see [85] for a discussion in the context of atom beams.

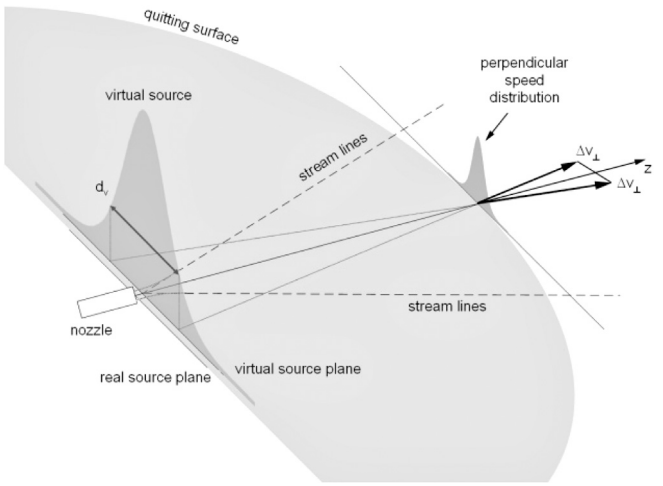

Fig. 7. Schematic diagram of a supersonic expansion and definition of the virtual source as the intensity distribution obtained by backtracking the direction of the atoms at the quitting surface to a minimum area: the virtual source. d_v is the full width half maximum of the virtual source. The stream lines indicate the direction of the atoms as they leave the nozzle. Eventually the beam enters molecular flow. This transition is approximated with the so called quitting surface. The perpendicular speed (velocity) distribution is indicated by $\Delta v_\perp$.
Source: The figure is reproduced from [92].

the definition of the quitting surface, which depending on the condition chosen, can be positioned before or after the skimmer aperture.

As mentioned above, the quitting surface can be integrated to obtain an analytical model for the beam intensity, this is known as the Sikora approximation [78]. This expression was initially calculated for a quitting surface placed exactly at the skimmer aperture and was later generalised by Bossel to incorporate a quitting surface placed before the skimmer [79]. This formula has been used to model measurements of centre line intensities [68] and in the optimisation of pinhole and single zone plate helium microscope configurations [97,102]:

$$I_S = I_{TG}\left\{1 - \exp\left[-S_i^2\left(\frac{r_S(R_F + a)}{R_F(R_F - x_S + a)}\right)^2\right]\right\}, \tag{6}$$

I_S is the intensity arriving at a detector of a given radius, r_D, downstream, the subscript "S" is included to indicate that the Sikora approximation is being used. x_S is the distance between the nozzle and the skimmer and a is the distance between the skimmer and the point where the intensity is measured. r_s is the radius of the skimmer and R_F is the radius of the quitting surface. The first term of the Sikora approximation I_{TG} is the intensity corresponding to a naive spherically-symmetric model of the supersonic expansion, where the atoms would travel in straight lines from the nozzle with equal probability at any angle and no thermal effects.[15] The radius of the detector, r_D, is included in this term. The total flow stemming from this ideal point source corresponds to the intensity resulting from the isentropic source model I_0. We name this factor the thermal-geometrical component, I_{TG}. The thermal-geometrical intensity measured at a detector of radius r_D at a distance a from the skimmer is then:

$$I_{TG} = \pi I_0 \frac{r_D^2}{(x_S + a)^2}. \tag{7}$$

This component suffices to understand a basic design principle of neutral helium microscopy: reducing the axial length of the microscope is often beneficial, as intensity will decrease with distance.

[15] The density at the skimmer can also be used, if the point source assumption is dropped [68].

The second term of the Sikora equation, the exponential term, models what we may term the thermal properties of the beam. The S_i indicates that depending on the microscope design the perpendicular ($\perp$) or the parallel ($||$) speed ratio dominates:

$$S_i = \sqrt{\frac{m\tilde{v}^2}{2kT_i}}, \qquad i = ||, \perp. \tag{8}$$

Here, T_i corresponds to the perpendicular or parallel temperature (as defined in Eq. (5)).

The fact that both the perpendicular and parallel speed ratios can be used in the same model of the beam intensity can be confusing. The reason behind this is that depending on where the quitting surface is assumed, one obtains an integral mostly dominated by the perpendicular speed ratio or by the parallel speed ratio — and therefore, different approximations apply. This was first demonstrated in [78]. The rule of thumb is the following: if there are reasons to assume that the quitting surface – understood as the position of last He–He collisions – is placed very close to the skimmer, the perpendicular speed ratio should be used and $R_F = x_S$. If the quitting surface is placed far before the skimmer then the parallel speed ratio should be used. The full derivation for this can be found in Appendix B of [78].

Recent experimental findings show a more complex picture: for small skimmers close to the quitting surface, using the parallel speed ratio in the Sikora model reproduces experimental measurements better (as perpendicular spread is not a big contributor given that very little of the quitting surface is seen at the detector). However, for larger skimmers seeing a thermalised portion of the expansion (for example, when the expansion is not assumed to end until significantly after the skimmer) the perpendicular speed ratio dominates as predicted by Sikora [68].

As mentioned above, the thermal-geometrical term I_{TG} describes a spherically symmetrical expansion. In reality as supersonically expanded atom beam decreases in intensity at a slower rate than a spherically symmetrical expansion. Thus the full Sikora–Bossel equation (Eq. (6)) gives a truer description of the phenomena at play. Let us look at this equation in the small skimmer limit:

$$I_S = I_{TG}\left\{S_i^2\left(\frac{r_S(R_F + a)}{R_F(R_F - x_S + a)}\right)^2\right\} \tag{9}$$

For a quitting surface at the skimmer $R_F = x_S$ we get:

$$I_S = I_{TG}\left\{S_i^2\left(\frac{r_S(x_S + a)}{a x_S}\right)^2\right\} = I_{TG}\left\{S_i^2\left(\frac{r_S}{a} + \frac{r_S}{x_S}\right)^2\right\} \tag{10}$$

This equation adds three important, physical corrections to the simple, spherical expansion expression (I_{TG}): (i) the beam will be more intense the wider the skimmer is — which accounts for thermal components of the quitting surface. (ii) Higher speed ratios means more intense beams — which is a measure of the quality of the supersonic expansion and of its departure from a spherically symmetrical expansion. (iii) the closer you are to the beam source, the more intense the beam will be compared to a spherically symmetrical expansion model. Note that (i) is still an approximation and only holds for small skimmers — if the skimmer size is on the order of the size of the quitting surface, increasing it further does not result in important intensity changes. The fact that the beam intensity decreases slower than in the spherical case, has design implications. It allows for larger and hence technologically more feasible microscopes. It is important to be aware of this when doing SHeM designs (see Section 6).

2.2.2. *Modified spherically symmetrical flux models*

Rather than integrating over the quitting surface/virtual source as described in the previous section one can obtain analytical expressions for the centre line intensity by using various additional approximations. In this section we review other intensity models that have been used for

SHeM and show how they compare to the isentropic, spherically symmetric expansion model, expressed by the thermal-geometrical term, I_{TG} (see Eq. (7)). The models that have been used for SHeM so far, have been inspired by centre line intensity derivations of Pauly [7], Miller [77] and dePonte [73] as well as Sikora (described above)

We start with models from the first type as described above, to which both Pauly and Miller belongs. These models approximate the intensity by considering a simple flow pattern: an isotropic[16] spherically symmetric expansion — such as what is assumed to obtain I_{TG}. The expression for the centre line intensity presented below is used to describe SHeM among others by [1,103]. Note that the expression differs from Pauly's calculation by a factor of approximately 2. We think that this is either because of a typo — the original Miller and Pauly's equations are identical. Or because they implicitly introduce the peaking factor that Miller introduces as being approximately 2 for helium [77], see also [71].

$$I = 0.155\frac{P_0}{k_B T_0}\left(\frac{2r_{nz}}{x_S + a}\right)^2 \pi r_D^2 \sqrt{\frac{5k_B T_0}{m}} = 0.62\sqrt{5/2}\frac{I_0}{f(\gamma)}\frac{r_D^2}{(x_S + a)^2} = 0.6077 I_{TG} \tag{11}$$

Where $f(\gamma) = \sqrt{\frac{\gamma}{\gamma+1}}\left(\frac{2}{\gamma+1}\right)^{1/(\gamma-1)} \approx 0.5135$. $\gamma = c_p/c_v$ is the heat capacity ratio, which is 5/3 for monoatomic gases and r_{nz} is the radius of the nozzle.

Secondly, we look at the expression used by Witham and Sanchez [2] to estimate the intensity in their pinhole microscope (see Fig. 4). Witham and Sanchez explicitly refer to Miller's derivation [77] for an isentropic intensity and they introduce a peaking factor κ in their calculations.

$$I = \kappa\frac{P_0 \pi r_{nz}^2 \left(\frac{\gamma-1}{2}+1\right)^{\gamma/(\gamma-1)}\sqrt{\frac{\gamma k_B T_0}{m}}}{kT_0}\pi\frac{r_D^2}{(x_S + a)^2} \approx 0.4871 * 2\kappa\sqrt{\gamma/2}\frac{I_0}{f(\gamma)}\frac{r_D^2}{(x_S + a)^2} \approx 1.1026 I_{TG}. \tag{12}$$

Note that both these equations do not include the skimmer radius. In the case of Witham and Sanchez this makes sense since they are modelling a microscope design that does not include a skimmer, however, experiments have shown that in systems with a skimmer, the size of the skimmer has to be considered [68].

Finally in [104] Bergin et al. model the source in a helium microscope using DePonte et al.'s centre-line beam intensity (with a correction) [73,104]. This is a model of the second type, in which an empirical formula for the dependency between the virtual source radius and the speed ratio of the beam is used (and therefore an inverse dependency on the speed ratio is introduced). The following formula (in flux per unit area) is used:

$$I_{berg} = \pi\beta^2 B = \pi\left(\frac{r_S}{x_S + a}\right)^2 B. \tag{13}$$

Where B is the brightness of the source (in number of atoms per steradian per unit area of the source). The following expression for B is provided:

$$B = 0.18\frac{P_0}{S_{||}\sqrt{mk_B T_0}}. \tag{14}$$

Combining both equations Bergin et al. arrive to a similar quadratic dependency with the skimmer radius as Sikora does in the limit of small skimmers (see Eq. (10)). Once rewritten in terms of I_{TG} and multiplied by πr_D^2 the intensity arriving at a detector downstream is recovered:

$$I = \frac{0.18\pi^2 P_0 r_S^2}{\sqrt{mk_B T_0}}\frac{r_D^2}{S_{||}(x_S + a)^2} = \frac{1}{S_{||}}\frac{0.18\pi}{\sqrt{2}f(\gamma)}\frac{I_0}{r_{nz}^2}\frac{r_S^2 r_D^2}{(x_S + a)^2} \approx \frac{0.247866}{S_{||}}\left(\frac{r_S}{r_{nz}}\right)^2 I_{TG}. \tag{15}$$

Here, r_S is the radius of the skimmer. Note how all three models have the same geometrical dependencies stemming from a spherically symmetrical expansion: the I_{TG} term. The intensity is then corrected upwards or downwards depending on further assumptions.

2.2.3. Skimmer effect

The intensity models discussed in the last section disregard any effect produced by the skimmer besides acting as an aperture. However, the reality is that skimmer interference is often a significant contributor to the beam's centre-line intensity [68]. In its journey, a helium atom can see its trajectory perturbed by atoms backscattered from the skimmer, or more generally a perturbation of the flow caused by it.

Modelling the effect of the skimmer is a well known challenge in helium beam experiments [72,74,83]. One of the most successful approximations to the problem is the one provided by Bird in the 1970s [82]. In this paper, Bird proposed the modified Knudsen number, and showed it to be a better predictor for skimmer interference than the Knudsen number. When designing a microscope, one should always aim for a modified Knudsen number larger than 1, as skimmer effects can decrease the intensity by as much as a factor 10 [68]. The modified Knudsen number for a Lennard-Jones potential reads:

$$Kn^* = Kn\left(\frac{2}{5}S_{||}^2\right)^{-1/6} = \frac{1}{r_S\sigma\sqrt{2n}}\left(\frac{2}{5}S_{||}^2\right)^{-1/6}. \tag{16}$$

Where Kn is the Knudsen number:

$$Kn = \frac{\lambda_0}{r_S} = \frac{1}{r_S\sigma\sqrt{2n}} \tag{17}$$

In here, the speed ratio term does not have any other effect than reducing the effective Knudsen number with respect to the standard Knudsen number. For a skimmer placed at a given distance x_S from the expansion, the true dominant factor is the skimmer radius r_S - smaller skimmers give larger Knudsen numbers. σ is the scattering cross-section of the atoms and n is the number density. In general, if one wants to control the optical properties of the beam, one must place the skimmer as close to the quitting surface as possible whilst having a radius that leads to a large enough modified Knudsen number.

Since the introduction of the modified Knudsen number and the DSMC calculations by Bird there have been several attempts at modelling skimmer interference without flow dynamics simulations. One of the attempts that managed to replicate experimental data the best was a numerical model by Hedgeland et al. [74]. In their paper, the authors propose that skimmer attenuation is mostly caused by the collision of backscattered particles with the central axis of the beam and provide a model to explain what they call an "anomalous attenuation" of the beam at low temperatures. Unlike previous attempts that relied on rather simplistic parameter fitting, [83], this model is based on a physical parameter: the backscattered atom's cross section, obtained from the solid angle of the beam.

Although this model is very promising and replicates well the experimental data reported by [74], it also predicts an inverse dependency of the atom's cross section with the solid angle of the beam. This means that the cross section would decrease for bigger skimmers (that are known to produce broader beams). However measurements published in 2018 [68] show that larger, equally streamlined, skimmers actually produce more interference than small skimmers — as predicted by the Knudsen number [68]. These new measurements cannot be explained by Hedgeland et al.'s model. Thus, it seems that researchers are still left with no other option than to model the full interference of the

[16] Note that isotropic is not the same as isentropic. Isotropic refers to the intensity being independent of the direction (spherically symmetric). Isentropic refers to the thermodynamic properties of the flow within the nozzle.

beam with the skimmer if they want to obtain precise predictions of the skimmer effect.

2.2.4. Background scattering

In addition to skimmer interference, helium atoms can interact with atoms scattered from any other element of the expansion chamber (also known as the background gas). Such interactions depend on the vacuum quality (pump capacity and in the case of a pulsed beam, size of the vacuum chamber) and can be modelled either through DSMC or through free molecular scattering. The latter is often preferred as it corresponds to a simple exponential law [68,74,83]:

$$\frac{I}{I_S} = \exp\left(-\sigma^2 n_{B_E} x_S - \sigma^2 n_{B_C} a\right) \tag{18}$$

Where σ is the scattering cross-section of the atoms and n_{B_E} and n_{B_C} are the background number densities in the expansion chamber and subsequent chamber. These background densities should be measured by a pressure gauge far away from the beam centre line.

3. Resolution limits

Once the centre line of the supersonic expansion has been selected by a skimmer, the helium atoms continue to travel in straight lines through vacuum until they interact with the microscope optical elements.

In this regime, the behaviour of helium atoms can be modelled by atom optics through the wave-particle duality. The wavelength, and thereby the resolution, is given by de-Broglie wavelength equation [105]: $\lambda_B = \frac{h}{p} = \frac{h}{\sqrt{2Em}}$. The mass of Helium is about four orders of magnitude higher than the electron mass. Thus, at the same energy, the de-Broglie wavelength of neutral helium atoms will be two orders of magnitude smaller than of electrons and thus the potential resolutions two orders of magnitude better. According to Eq. (3) a room temperature helium beam has a wavelength of around 0.05 nm and an energy of around 60 meV [12]. A beam cooled with liquid nitrogen and working at 120 K has a wavelength of around 0.1 nm and an energy of around 20 meV. However, the practical resolution limit of a Helium microscope configuration is not given by the theoretical wavelength limit, but by aberrations and diffraction (Airy disk) broadening by the optical elements and by the signal to noise ratio in the detected signal. As discussed in the introduction, two types of optical elements have been used so far to successfully produce SHeM images: Fresnel zone plates and pinholes. Fresnel zone plates are a type of diffraction lens that focuses an incoming atomic or light beam into a small focal spot [18].

When referring to resolution, it is important to distinguish between the lateral resolution, determined by the size of the helium beam, and the "angular resolution", given by the solid angle covered by the detector opening. The lateral resolution is what impacts the minimum feature size that can be observed and therefore is referred to in the field as "resolution". Diffraction with detecting apertures does not degrade the lateral resolution as in light optics, because helium microscopes image by measuring the flux through the aperture and not by projecting the image onto a sensor plane. Angular resolution determines the intensity of scattered helium in a particular direction. This is mainly of relevance for contrast, in particular for 3D imaging, as multiple scattering makes it difficult to image high aspect ratio structures [106,107].

In 2018 the concepts supra- and sub-resolution were introduced to helium microscopy [108]. Supra resolution is the same as the lateral resolution, determined by the size of the helium beam. Sub resolution is the contrast effect, which occurs because the helium atoms are sensitive to the atomic scale roughness of the surface. This will be discussed in more detail in Section 4.

The difference between the resolutions of Fresnel zone plates and pinhole microscopes is given by the contributions of diffraction (Airy disk) and aberration terms [109]. The square of the Full Width at Half Maximum[17] for the zone plate (Φ_{ZP}) and the pinhole (Φ_{PH}) microscope can be written as:

$$\Phi_{\mathrm{PH}}^2 = O_{\mathrm{S}}^2 + \sigma_A^2 \tag{19}$$

$$\Phi_{\mathrm{ZP}}^2 = O_{\mathrm{S}}^2 + \sigma_A^2 + \sigma_{\mathrm{cm}}^2. \tag{20}$$

Where O_{S}^2 indicates the geometric optics contribution to the full width half maximum. That is to say O_{S}^2 is the image of the source at the sample. For the zone plate microscope it is the demagnified image of the skimmer or the source limiting aperture [110], σ_A is the Airy disk contribution from edge diffraction from the zone plate or pinhole and σ_{cm} is a chromatic aberration term that appears for the case of the zone plate. The first equation holds under the assumption that the Fresnel number is smaller than 1, which is the case for the limit of small pinholes. For a Fresnel number larger than 1 only the geometric optics term plays a role [102].

Besides the de-Broglie wavelength, there is no theoretical limit as to how small O_S can get. However, for the case of a pinhole, σ_A is proportional to $1/r_{ph} \propto 1/O_S$ [102], where r_{ph} is the radius of the pinhole, thus the Airy term increases when one tries to decrease O_S. For the zone plate the situation is more complex, because of the additional chromatic aberration caused by the velocity spread of the helium beam. The chromatic aberrations in a zone plate are proportional to its radius r_{zp}, while its Airy term depends linearly with the width of the outermost zone Δr: $\sigma_A \propto \Delta r \propto O_S$ [97]. In other words, for a fix zone plate radius both the resolution and the Airy contribution decrease linearly with the same factor. This allows zone plates to reach significantly higher resolution (smaller spot size) than pinholes [97,104], see also Section 6.

The resolution limits for both instruments can be explicitly obtained (see [97,102]). For a pinhole microscope:

$$\Phi_{PH}^{min} = K\sqrt{0.42\lambda W_{\mathrm{D}}\sqrt{3}}. \tag{21}$$

Where $K = 2\sqrt{2\ln 2/3}$ and W_{D} is the working distance (the distance between the optical element and the sample). The 0.42 factor comes from the Airy disk standard deviation [111]. In a zone plate microscope the minimum possible resolution (minimum size of the focused spot) is given by the width of the smallest zone (as the optical and Airy terms both linearly depend on Δr).

$$\Phi_{ZP}^{min} = K\sigma_A \approx \Delta r. \tag{22}$$

This is a well-known result from light optics for the first order focus [109]. For higher orders the focused spot size can be smaller than the width of the smallest zone [109]. This sounds promising at first, but given that only a fraction of the beam enters into the focus (max 12.5% for the first order focus and much less for the higher orders) using a higher order focus is not an option with present detector efficiency (see Section 5). In practice, this means that the resolution is limited by nanofabrication. It is difficult to make very small free-standing zones. For this reason, experiments have been done on a so-called atom sieve zone plate configuration. The atom sieve is a zone plate superimposed with a hole pattern. The fabrication limit is now determined by how small free-standing holes can be made, rather than by how small free-standing zones can be made. In fact, the resolution limit will be even smaller than the smallest free-standing hole, because the design can be made so that a hole covers two zones and the resolution limit remains the width of a zone Δr. The idea is adapted from photonics [112]. The first focusing of helium atoms using an atom sieve was done in 2015 [113] see also [114]. As a final remark we can mention that it has been shown that the Beynon Gabor zone plate performs similar to a Fresnel Zone Plate [115]. The Beynon Gabor zone plate was previously cited in the literature as having a higher intensity in the first order focus

[17] The full width at half maximum of the beam's intensity profile [102].

that the Fresnel zone plate, however this turned out to be an artifact due to lack of sampling nodes.

Finally it should be noted that the fabrication limit of the width of the outermost zone of the zone plate introduces a minimum for W_D for a given zone plate radius. From [109] we have the following relation, where f is the focal length of the zoneplate and the approximation is done under the assumption that a is large so that $f \approx W_D$:

$$\Delta r = \lambda f / 2r_{zp} \approx \lambda W_D / 2r_{zp} \rightarrow W_D = 2r_{zp}\Delta r / \lambda \tag{23}$$

The discussion of resolution so far has been based on the full width at half maximum of the beams intensity profile on the sample. This is a useful working number, but does not directly correspond to the smallest feature that can be resolved. Recently Bergin et al. proposed a procedure for measuring the resolution in scanning helium microscopy using test samples with sets of slits of well-defined dimensions to establish a quantitative resolution criterion in SHeM instrumentation [116]

4. Contrast properties

The first paper dedicated to the concept of contrast in SHeM was published in 2004 by MacLaren and Allison. It discusses what contrast mechanisms are to be expected on the basis of the theory of helium scattering [3].

The general theory of helium scattering has been treated in a range of books and review articles, see for example [10–13]. Unlike electrons, X-rays and neutrons which all interact with the core electronic cloud and atomic nuclei in the sample, thermal helium atoms scatter off the outermost electron density distribution at the sample surface. The classical turning point for helium is a few Ångstroms above the surface [117]. It is no surprise therefore that the helium beam is very sensitive to surface defects such as adatoms, vacancies and atomic steps. Experimental results on metal surfaces have shown that a defect coverage (defined as the ratio between the number of adparticles and the number of surface atoms, both per unit area) of $\ll$ 1% of a monolayer can be detected [118–120]. The helium specular intensity (see below) decreases as a function of defect coverage, similarly to how a beam which crosses a gas-filled scattering cell has its centre line intensity reduced by collisions with gas atoms. The lost intensity turns into diffuse intensity. This analogy allows the introduction of the concept of an effective cross section for defects. The cross section of a single adatom as seen by helium is typically 100 Å^2 which exceeds by far the atomic diameter. Even for hydrogen, the cross section is estimated to be of the order of 10 Å^2 [121].

To understand these large cross-section values, it is necessary to analyse the scattering mechanism and in particular the helium-surface interaction potential. This interaction can be separated into a short range repulsive part, due to the overlapping of the electron densities of helium and the surface electron density, and a long range attractive part, due to the van der Waals interaction. The repulsive part taken on its own, gives a cross section of the order of the atomic size, but including the attractive interaction which modifies the atom trajectories already far from the surface, increases the estimated cross section value to reach the experimentally measured values. As the coverage increases, the effective cross sections of different defects start to overlap [122,123].

The main different helium scattering processes that can occur are illustrated in Fig. 8. The first major distinction is between elastic and inelastic scattering. In the case of elastic scattering, the energy of the helium atom is unchanged during the scattering process. In inelastic scattering an energy exchange with the surface takes place through phonon creation or annihilation.

Specular scattering is elastic scattering, where the outgoing scattering angle is equal to the incident scattering angle. In the case where the roughness (variation in slopes) is on a length-scale bigger than the instrument resolution (focused spot size), the direction of the specularly

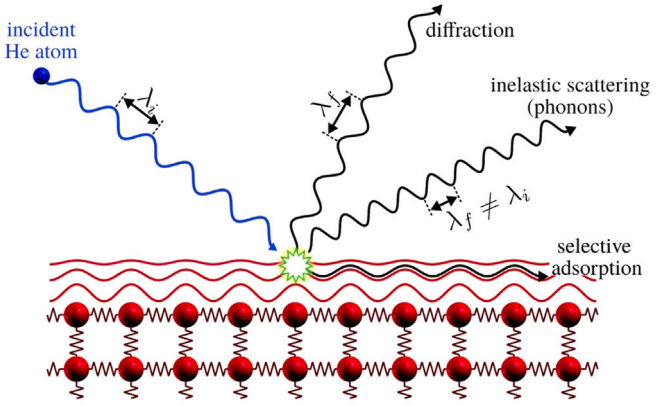

Fig. 8. Illustration of the different processes for the scattering of He atoms on a surface. For crystalline surfaces diffraction is included. The helium atom scatters off the electron density distribution, indicated as red lines, without any penetration into the bulk. Selective adsorption refers to the trapping of a helium atom in the helium surface interaction potential. Here λ_i and λ_f denote the wavelength of the incident and scattered helium atoms, respectively. Inelastic scattering leads to a wavelength change. *Source:* Figure reproduced from [11].

scattered beam will vary. This is referred to in the SHeM literature as topographical contrast. In the extreme case, when the surface is so rough on the atomic level that it acts as a perfect elastically diffuse scatterer (see Section 4.1) the reflected signal will be independent from the incident beam direction, but still depend on the local, average surface normal. This is also referred to as topographical contrast. Roughness on the atomic level can occur through the presence of atomic defects, as discussed above. In the intermediate case, where the roughness is smaller than the instrument resolution but the surface is not a perfect diffuse scatterer, the specularly reflected beam will broaden. This broadening provides a measure for the roughness variation down to the scale of the wavelength of the helium atoms (Ångstrom scale). This broadening effect has recently been referred to in the SHeM literature as sub resolution contrast [124]. First observation of sub resolution contrast can be found in [2] It provides a unique method for fast, large area evaluation of nano-coatings [69,125].

As mentioned above the helium atoms have a wavelength on the Ångstrom scale, which is comparable to the atomic spacing in materials, so if the substrate is crystalline with a corrugated surface electron density distribution and reciprocal lattice parameters matching the k-vector component of the helium atom parallel to the surface, elastic scattering can occur in the form of diffraction. Such diffraction contrast in SHeM was observed for the first time in 2020 [126], through imaging of a Lithium Fluoride crystal sample. Elastic scattering can also occur as resonant state scattering, also referred to as selective adsorption resonance, which occurs when the helium atom is trapped in the helium-surface interaction potential, however, this is generally a rare phenomena and has not been considered as a contrast forming process in SHeM up till now.

Finally, and not shown in the figure, we have the case where a surface is very rough relative to the wavelength of the atoms or has a deliberately imposed high aspect ratio structure. Here the atoms may undergo more than one (elastic or inelastic) collision with the surface, which gives shadowing effects. Multiple scattering contrast was first discussed in [57], where it is highlighted that the detector can be seen as being "the source of the illumination", similar to Scanning Electron Microscopy and Focussed Ion Beam imaging, where shadowing effects are also observed. Multiple scattering contrast is described in [106], see also [107]. In the extreme case, when the atoms are thermally equilibrated with the surface through the multiple scattering, the scattering profile will be spatially similar to that of a perfectly elastically diffuse scatterer, see Section 4.1.

Inelastic helium scattering has been investigated for many years using so called time of flight experiments, where the beam is chopped into short pulses and the creation and arrival time of each pulse measured, so that the time of flight (TOF) for each pulse can be converted into energy of the atoms and thus used as a measure for energy transfer with the surface — annihilation or creation of phonons. So far, however, no SHeM has been equipped with TOF.

For inelastic scattering, we distinguish between the single phonon and multi phonon regimes, also referred to as the quantum and classical regimes. In the single phonon regime, the helium atoms excite or de-excite individual phonon vibration modes. The single phonon regime occurs when single phonon annihilation or creation is the dominant inelastic process and the probability of exciting two or more phonons is small.

In the multi phonon regime several phonons are excited at the same time. This situation occurs if the vibration energies for the surface molecule charge oscillations are much lower than the energy of the incident helium atoms (the helium atoms see the surface molecules as "floppy"). In this case there will not be discrete excitations. Thermal vibrations of the surface atoms leads to an increase in multiphonon scattering with temperature.

Inelastic scattering will lead to a loss in the elastically scattered signal. The intensity loss in the multiphonon regime I/I_0 is described by the Debye–Waller factor (DWF). The Debye–Waller factor was first introduced in X-ray scattering. For helium scattering it has the form (note the temperature dependence) [127]:

$$\frac{I}{I_0} = exp(\frac{-24mT(E_i cos^2\theta_i + D)}{Mk{\Theta_D}^2}) \tag{24}$$

where E_i is the incident energy of a helium atom, m the mass of a helium atom, M the surface atomic mass, θ_i the incident angle of the beam on the surface and T the surface temperature and Θ_D the Debye temperature, D is the well depth of the helium surface interaction potential and k is the Boltzmann constant.

Eq. (24) shows that inelastic scattering offers the possibility of chemical contrast, since different chemical compounds on the surface will lead to different surface atomic mass, Debye temperature and well depth of the helium surface interaction potential. The first indication of chemical contrast stems from 2015 when Barr et al. published the SHeM images shown in Fig. 9 [127]. They suggest that the remarkable contrast difference one observes in these images is due to the fact that different chemical elements (different metals) are being imaged. It is argued that since helium can probe subsurface resonances, chemical contrast can be provided even in the presence of multiple adsorbate layers. As an argument that the contrast is truly chemical and not sub-resolution contrast caused by differences in surface roughness, the SHeM images are compared with AFM images. It is argued that the observed SHeM contrast does not follow the root mean square roughness trend in the AFM data. One may make the remark here, that roughness is in truth a spectral density function and determined by the "ruler" used to measure it. For AFM this is the tip diameter – several nanometers, for SHeM the wavelength of the helium atoms – less than one nm. Thus one cannot necessarily expect the roughness measured with the two methods to be comparable.

In reality, several contrast mechanisms will often be at play at the same time. Contrast mechanisms are explored in [128] and [69], where imaging has been done using helium beams seeded with argon and krypton. Seeded helium beams is a well established technology, used among others for thin film deposition, see for example [129]. In a microscopy context the seeded beam technique makes it possible to obtain images simultaneously with different atomic species. In principle this should make it possible to separate the different contrast mechanisms at play since, using Eq. (24) with different masses, m and E_i. A clear contrast difference is indeed observed between the imaging with the two different gasses in [128] and [69]. In practice, however, the contrast difference is not so easy to explain because not only the mass but also the interaction potential with the surface, and thereby the well depth, D will vary. It should also be noted that the seeded beam imaging cannot be used in the zone plate configuration, since atoms with different masses at the same velocity will have different de-Broglie wavelengths.

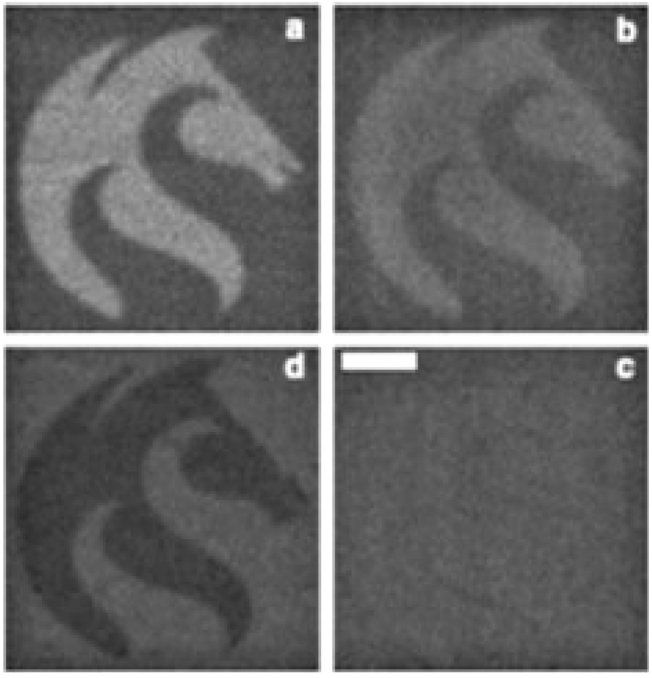

Fig. 9. SHeM images showing the University of Newcastle logo in different metals on a silicon substrate. Clockwise from top left: (a) gold, (b) nickel (c) platinum and (d) chromium. Scale bar, 50 μm from the difference in contrast can be contributed to the sensitivity of the helium beam to the atomic scale roughness of the different metal films (the so called sub resolution contrast, see main text for further discussion). The possibility of chemical contrast is also discussed in the original publication.
Source: From [127].

4.1. Contrast modelling

So far theoretical modelling of contrast properties has focused on topographical contrast only. Three different approaches have been used: One model assumes perfectly diffuse elastic scattering (Lambertian scattering), a second model (Knudsen flux scattering) assumes perfectly diffuse inelastic scattering, with the scattered atoms equilibrated to the surface temperature through multiple scattering. The two first models have the same spatial scattering distribution. The intensity, I_{Ω_D} seen at a given solid angle Ω_d for Lambertian or Knudsen flux scattering is given as [102]:

$$I_{\Omega_d} = I_{inc}\cos(\pi/4)\Omega_D = I_{inc}cos^2(\pi/4)\frac{\pi R^2}{d^2} \tag{25}$$

where I_{inc} is the intensity per solid angle, R is the radius of a circular detector opening at a distance d from the sample.

The third model assumes specular (elastic) scattering from individual slopes. The third model will approach the two others with increasing surface roughness.

The two first publications of theoretical methods for calculating resolutions in SHeM's assume Lambertian reflection for modelling the scattering [97,102]. The term Lambertian reflection is taken from light optics, and corresponds to scattering from a perfect, diffuse reflector. The scattered lobe has a $\cos\theta$ spatial distribution with respect to the surface normal. The light does not change its wavelength (energy) during scattering. In other words, the scattered lobe is independent of the energy and angle of the incident beam.

The second scattering model is Knudsen flux scattering, which has the same $\cos\theta$ scattering distribution as Lambertian reflection [130], see also [126]. There is a fundamental difference however, between Lambertian reflection and Knudsen flux scattering. In Lambertian reflection the light does not change its wavelength (energy). This is not the case for the Knudsen flux scattering. Knudsen scattering is the scattered (desorbed) distribution, when the incident beam is totally adsorbed on the surface into the physisorption well, and then remains in the well long enough to equilibrate to the surface temperature, and then ultimately leave the surface via desorption [131] or alternatively for rough surfaces, equilibrate to the surface temperature through multiple inelastic scattering events.

The conditions for obtaining what we refer to as Knudsen flux scattering have undergone an interesting debate. Initially, the Knudsen flux was thought to be the flux of particles that would pass through an imaginary flat plane placed in an equilibrium gas. However, this derivation was shown to be flawed by Wenaas [132]. In 2004 Feres and Yablonsky showed that Knudsen scattering was one[18] of the expected results of a random billiard model for gas-surface interactions. This remains as one of the most convincing explanations for Knudsen scattering [133].

The $\cos\theta$ distribution is used in [134]. Here the scattering is simply labelled as diffuse scattering. It is not clear whether the Lambertian or the Knudsen flux scattering is referred to, however the result is the same as explained above. In a very recent paper a systematic study of diffuse scattering from microspheres of different materials, show that all investigated materials display an approximate cosine distribution [135].

In [106] multiple elastic scattering is included in the modelling of images of samples with high aspect ratios.

The last approach, referred to as the third model at the beginning of this section, has been to model the scattering from rough surfaces as elastic scattering from a surface consisting of a distribution of slopes, obtained from independent AFM images [125]. The samples imaged were macroscopically flat and the explicit aim was to investigate the roughness on the (sub)-nanometer scale. The samples were moved from air to the vacuum chamber and imaged directly in its native state without any cleaning. Ref. [125] is the first paper to combine SHeM with helium atom scattering time of flight studies on reference samples. The Time of Flight measurements show that the average velocity of the helium atoms does not change during the interaction with the surface (as would have been the case if Knudsen flux scattering had been dominant). This is the first experimental evidence of contrast generated mainly through diffuse elastic scattering. The shape of the TOF spectra are very similar for all the surfaces investigated (gold, glass, silicon an diamond). The paper suggest that this is due to the surfaces being investigated without any surface cleaning, which means that they will all be covered in adsorbates (water, CO etc.).

5. Detection

Detection remains the single biggest challenge in neutral helium microscopy. The big advantage of the technique — the inertness, low energy and surface sensitivity of the helium probe is its biggest disadvantage when it comes to detection. Up till now three types of neutral helium detectors have been used and/or investigated for SHeM experiments: (i) Pitot-tube detectors — an accumulation (stagnation) detector, where the pressure increase from the helium flow into a small chamber is measured with a pressure gauge [50,110] (electron bombardment without mass selection). (ii) electron bombardment detectors with mass selection [128,136–145], and (iii) field ionisation detectors [73,146–151]. Bolometers [152] have been used extensively in helium atom scattering experiments and photon resonance has been applied to ionise helium [153,154], but these approach have not been used in SHeM so far.

Field ionisation detection is in principle a very attractive method, because it offers the possibility of extreme spatially resolved detection. The potential of field ionisation is demonstrated in helium ion microscopy, which uses field ionisation to generate a helium ion source, spatially confined to one ionising atom. In an early helium microscope design proposal the sample is broadly illuminated and a mirror focuses the reflected beam onto a field ionisation detector [155]. So far a SHeM with field ionisation detector has not been built. One reason for this is that the field ionisation probability is strongly dependent on the velocity of the helium atoms and so would require a strongly cooled beam to achieve a reasonable detection efficiency [148,149]

Up till now all SHeMs have used electron bombardment detectors. Helium has the highest ionisation potential of all species: around 24.6 V[19]. A key component in a helium electron bombardment detector is therefore the ioniser. Here, electrons are emitted from a negatively biased filament and accelerated by an acceleration voltage, which must be greater than 24.6 V, towards the helium beam. Positive helium ions are then created through collisions with the high-energy electrons.

Once the helium atoms have been ionised, they need to be detected. In the simplest configuration this is done with a so-called Pitot-tube setup, used among others in [50,110] for microscope characterisation experiments. The helium beam goes through a narrow tube into a small unpumped chamber. The intensity of the helium beam is then measured by recording the pressure increase in the small volume, see [101] for a description of a practical implementation. The Pitot-tube detector is very inefficient and can in practice only be used for transmission experiments, where the recorded beam intensity will be high.

A much more efficient detection is achieved by mass separation: designed to select only those ions that interest us (helium ions coming from the beam). In SHeM (and HAS) this is often done using magnets [145,156] rather than the quadruple mass filters typically used in commercial residual gas analysers (mass spectrometers) [157], because the magnets yield higher recorded intensities for helium. A magnet-based detector was used for the first (transmission) SHeM images [48]. A description of the design can be found here [136]. The helium atoms are directed from the ioniser to the mass separation stage and from the mass separation stage to the signal multiplier using ion optics [128,145,158]. The signal multipliers used in SHeM are electron multipliers, typically tube-based multipliers known as channeltrons [159].

A lot of time and energy has been spent on increasing the efficiency of neutral helium detectors. Especially promising are detector systems based on solenoidal ionisers, with recent work reaching an efficiency of as much as 0.5% [145] - the highest obtained to date and around three orders of magnitude higher than for the detector used in the first helium microscopy experiments [136]. Another promising development is a recent framework aimed at optimising the balance between signal and temporal response in neutral helium detectors. The basic idea is to use adjustable stagnation to obtain a larger helium signal, with a reported signal improvement of 27% [160].

5.1. Signal to noise ratio

Unfortunately a high ionisation efficiency for helium is not the only requirement for a powerful SHeM instrument. An equally crucial parameter is the signal to noise ratio, which sets a limit for the smallest signal that can be detected in a given measurement time. For electron bombardment detectors, the only detector type used in SHeMs so far, as mentioned above, there are two factors that contribute to the noise:

Firstly there is a contribution of ions from other species present in the background gas. Species such as H_2, H_2O, CO and CO_2 will

[18] But not the only one, other distributions are also possible.

[19] https://physics.nist.gov/PhysRefData/Handbook/Tables/heliumtable1.htm

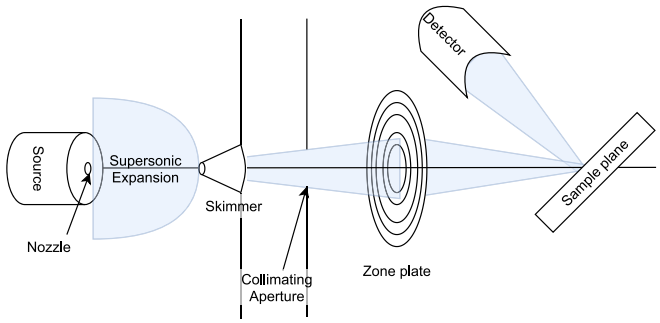

Fig. 10. Simplified diagram of the zone plate microscope setup in reflection.

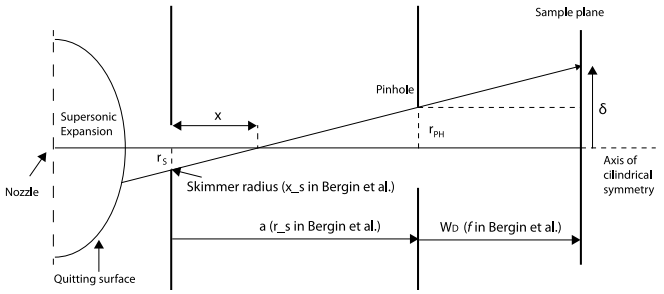

Fig. 11. Sketch showing the pathway of the beam onto the sample for a pinhole microscope. The figure illustrates how the beam is limited by the skimmer in the Salvador et al. approach. The geometrical optics image of the skimmer is projected onto the sample plane through a pinhole, giving an image of the skimmer with radius δ.

always be present, because the vacuum is not perfect. These species all have a much lower ionisation potential than helium. Most of the ions generated will be withheld by the mass filter, but in the case of for example triple ionisation of carbon, they will be mass selected. Multiple ionisation can be strongly reduced by keeping the energy of the ionisation energy as low as possible, a good vacuum also helps in general, but even so a contribution from the background gas cannot be completely prevented.

Secondly, there will be a background contribution from the helium probe itself. The part of the helium beam which is not directly reflected into the detector by the sample, will be scattered in the rest of the chamber and reflected off the walls, thus creating an additional background of helium in the chamber. A fraction of this helium background will reach the detector. Praxis has shown that this helium background usually is the dominating contributing factor to the noise in SHeMs. The magnitude of the background will depend on factors such as pumping speed and detector opening area. It can be reduced by using a modulated beam (chopped beam) as has been demonstrated with many other techniques, however so far this has not been implemented in SHeM. This is a very hard task since the requirement of high efficiency for the detector is generally obtained at the expenses of the response time which is lengthened, whereas modulation techniques require a relatively fast time response. This is more specifically discussed for SHeM in [57], see also [160].

6. Optimal microscope configurations

The difficulties associated with detecting neutral helium atoms have prompted several researchers to try to optimise the design of helium microscopes to obtain a maximum beam intensity for a given resolution.

To date, there are four papers that aim to optimise the microscope design using a theoretical framework for the beam intensity. The first paper from 2016, written by Kaltenbacher [103] presents an approach to optimise a microscope composed of a pinhole and two zone plates. However, Kaltenbacher does not consider the dependency of the beam centre-line intensity with the skimmer radius, rendering his approach not reliable in terms of the intensity. The next two papers from 2016 and 2018 [68,102], by Salvador et al. present analytical approximations for calculating the optical configurations for pinhole and single zone plate SHeMs in terms of resolution and intensity. In addition, the system is also solved numerically. The zone plate configuration optimised can be found in Fig. 10. The pinhole configuration has already been shown in the introduction, Fig. 5.

The last paper on microscope optimisation by Bergin et al. from 2019 [104] also presents optimisations of a pinhole and a single zone plate microscope including numerical simulations. It reaches the same qualitative conclusions on beam design as the two previous papers. The differences in the approaches of Bergin et al. and Salvador et al. are that Salvador et al. model the source using the full Sikora model (Eq. (6) in this paper) whereas Bergin et al. use a simplified approximation of the Sikora model (Eq. (15) in this paper). Both approaches models the beam as a Gaussian distribution with a standard derivation σ corresponding to the skimmer radius, but Salvador et al. includes an additional limitation of the beam by the skimmer diameter as in geometrical optics, see Fig. 11. Furthermore Salvador et al. use derivation to solve the optimisation problem, whereas Bergin et al. use Lagrange multipliers.

Both Salvador et al. and Bergin et al. provide analytical expressions for the optimal pinhole size in a pinhole microscope configuration. Salvador et al. produce a solution valid for any working distance (W_D), while Bergin et al. implicitly assumes $W_D \ll a$, where W_D is the microscope working distance (distance between pinhole and sample plane, f in the original Bergin et al. paper) and a is the distance between the skimmer and the pinhole (r_s in the original Bergin et al. paper), see Fig. 11.

Salvador et al. obtain the following solution for the optimal pinhole radius r_{PH}^{opt} (Eq. (18) in the original paper [102]).

$$r_{PH}^{opt} = \frac{\Phi_{PH} \cdot a}{2K(a + W_D)} \overset{W_D \ll a}{\approx} \frac{\Phi_{PH}}{2K}. \tag{26}$$

where Φ_{PH} is the Full Width at Half Maximum of the beam at the sample plane (the resolution, see Section 3) and $K = \sqrt{8\ln(2)/3}$. We see that the diameter of the pinhole is always smaller than the Full Width Half Maximum of the beam at the sample plane. For the case $W_D \ll a$ the solution becomes independent of both W_D and a.

Bergin et al. obtain the following expression for the optimal pinhole diameter, d_{PH}^{opt}, (Eq. (25) in the original paper [104]):

$$d_{PH}^{opt} = \sqrt{6}\Phi_{PH}^{\sigma} \approx 2.5\Phi_{PH}^{\sigma}. \tag{27}$$

Where Φ_{PH}^{σ} is the standard deviation of the helium beam at the sample plane. Since both approaches model the beam as a Gaussian distribution we have $\Phi_{PH} = 2\sqrt{2\ln 2}\Phi_{PH}^{\sigma}$. The solution of Salvador et al. for $W_D \ll a$ in terms of Bergin et al. parameters thus becomes:

$$d_{PH}^{opt} = 2\sqrt{2\ln 2}\Phi_{PH}^{\sigma} / \sqrt{8\ln(2)/3} = \sqrt{3}\Phi_{PH}^{\sigma} \approx 1.7\Phi_{PH}^{\sigma} \tag{28}$$

For a zone plate configuration, no analytical expression for the optimal standard deviation of the helium beam at the sample plane Φ_{ZP}^{σ} has been obtained. The optimal distance between the skimmer and the zone plate a was found in [97] to be described by the cubic equation:

$$a^3 + 2a^2\left(R_F - \sqrt{3\Gamma}r_{zp}\right) + aR_F(R_F - 4r_{zp}\sqrt{3\Gamma}) = r_{zp}\sqrt{3\Gamma}R_F^2\left[\frac{2S^2\Phi'^2 + r_{zp}^2(\Gamma - 1)}{S^2\Phi'^2 - 0.5r_{zp}^2}\right]. \tag{29}$$

Where $\Gamma \equiv \frac{1}{3}\left(\frac{2\Delta r}{\lambda}\right)^2$ is a constant of the problem which gives the relative size of the smallest zone, Δr, of the zone plate with a given

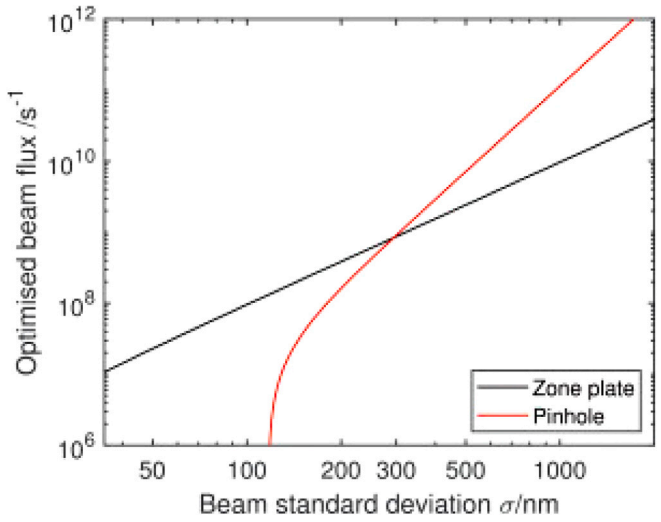

Fig. 12. Plot of the optimised beam intensity (flux) versus beam standard deviation (σ) at the sample plane. σ is a measure for the resolution, Φ, which is defined in Section 3 as Full Width Half Maximum of the beam at the sample plane. For a Gaussian beam we have: $\Phi = 2\sqrt{2\ln 2}\sigma$. We see that for lower resolutions the pinhole microscope performs better, but as the resolution improves it is outperformed by the zone plate microscope. For the configuration optimised here, based on a working distance of 1 mm and a wavelength of $\lambda = 0.056$ nm, resolutions better than around 200 nm are only possible with a zone plate microscope. Figure reproduced from [104], where details regarding the optimisation parameters can also be found.

radius r_{zp} compared with the average wavelength of the beam, usually $\Gamma \gg 1$. S is the speed ratio in Eq. (6). R_F is the radius of the quitting surface and $\Phi' = \sqrt{\left(\frac{\Phi_{ZP}}{K}\right)^2 - \sigma_A^2}$ is the corrected focal spot size (the focal spot size minus the diffraction term given by the smallest zone).

The work done on optimal SHeM configurations has had major impact in microscope design. Most importantly, it has proven that for a given working distance (distance between optical element and sample) and given distance between skimmer and optical element, the zone plate microscope provides higher intensities at higher resolutions than the pinhole microscope (see Fig. 12). This is not an obvious insight, given that only around 12.5% of the beam incident on the zone plate enters the focused beam spot (see Section 3), whereas 100% of the beam that passes through the pinhole contributes to the beam spot.

While Fig. 12 shows that the zone plate microscope eventually "beats" the pinhole microscope for a given working distance, it is important to note that the zone plate imposes a minimum size for the working distance, see Eq. (23), which is not present for the pinhole microscope. Furthermore, for the zone plate microscope to work well, an order sorting aperture needs to be inserted between the zone plate and the sample as previously discussed [50]. In general, the smaller the distances the higher the intensity, so if the working distance is not an issue, it may be possible to conceive a pinhole design which gives higher intensity for a given resolution than a corresponding zone plate microscope. The best resolution in SHeM so far: 0.315 μm was obtained using a pinhole microscope with a working distance of 10 μm [57], two orders of magnitude less than what was used in Fig. 12.

6.1. Microscopes with micro-skimmers

Initial designs of helium microscopes used skimmers as small as technically feasible (a few μm or less). This was motivated by the desire to obtain focal spots as small as possible and micro-skimmers seemed the best way to go in the zone plate/focusing mirror set up. The first supersonic Helium beams with micro-skimmers were created by Brown et al. in 1997 [72]. Micro-skimmers are made by controlled drawing of glass tubes produced according to techniques developed for patch-clamp probing of cells. Brown et al. observed a broadening of the speed ratio in micro-skimmers compared to standard skimmers and suggested that this was due to geometrical imperfections and/or imperfections at the lip edge. It was recently shown that it is possible to obtain the same speed ratios from micro-skimmers and standard skimmers [70].

Eventually it became clear that the centre-line intensity from micro-skimmers was a limiting factor for the signal intensity in the imaging spot, and a systematic study of the influence of the skimmer size on the centre-line intensity was conducted [68], using skimmer diameters of 4, 18, 120 and 390 μm diameters and in addition two flat apertures with diameters 5 and 100 μm. Some further measurements using a 50 μm diameter skimmer can be found in [66]. The results obtained from [68] was one of the incitements for the work on microscope optimisation discussed above. Here it is confirmed that the dependency of the centre-line intensity with the skimmer radius plays an important roles for the imaging spot intensity [97,102,104].

Since then, new SHeM designs of both pinhole and zone plate configuration, use skimmers as big as possible given available pumping speed in combination with collimating apertures in front of the skimmer, taking into account skimmer interference at large Knudsen numbers as mentioned in Section 2.2.3. This has the additional advantage that it enables fast resolution change by switching between different collimating apertures *in situ* [110].

6.2. Imaging with other atomic and molecular beams

As discussed in the introduction and in Section 4 imaging experiments have been carried out using other atomic and molecular beams than helium. Transmission experiments were done using deuterium [51], and reflection imaging has been done with krypton [58, 69] and argon [128]. In the case of [128] and [69] the imaging was done using so called seeded beams - a mixture of helium with the other gas. As discussed in Section 4 this leads to a situation where the sample is imaged with two probes of about the same velocity (see Eq. (4)) but different kinetic energy due to the different mass. For the case of a pure He beam at 65 meV, reducing the He fraction to 90% adding 10% of Kr changes the He beam energy to 22 meV while the Kr has an estimated energy of 453 meV, for a mixture of 50% He and 50% Kr the energies are 6 meV and 124 meV, respectively [69]. As also discussed in Section 4 this (together with the change in interaction potential) lead to a difference in contrast. Interestingly this strong difference in contrast was not seen in [58], where imaging was done with two separate beams of helium and krypton both at the same temperature maybe due to the similar incident energies of the beams.

We here briefly discuss the advantages and disadvantages of using other substances than helium for imaging: For a given energy larger atoms (i.e. argon and krypton) have a smaller de Broglie wavelength than helium. This is an advantage for a pinhole microscope because it reduces the diffraction at the pinhole which sets the limit for the resolution, see Eq. Appendix A. Regarding detection, heavier atoms are easier to ionise than helium which is an advantage. For a zone plate microscope the smaller wavelength is a disadvantage, since the zones becomes smaller and hence more difficult to fabricate. Furthermore, helium has unique properties which makes it possible to produce supersonic expansion beams with a narrower velocity distribution than what can be achieved with other atoms [161]. A narrower velocity distribution reduces the chromatic aberrations in a zone plate microscope.

7. 3D imaging

A very interesting perspective for SHeM is the potential to do true-to-size 3D imaging on the nanoscale: a nano-stereo microscope. The first 3D helium microscopy images were obtained by Myles et al. [162] in 2019. The 3D images were obtained by measuring the displacement

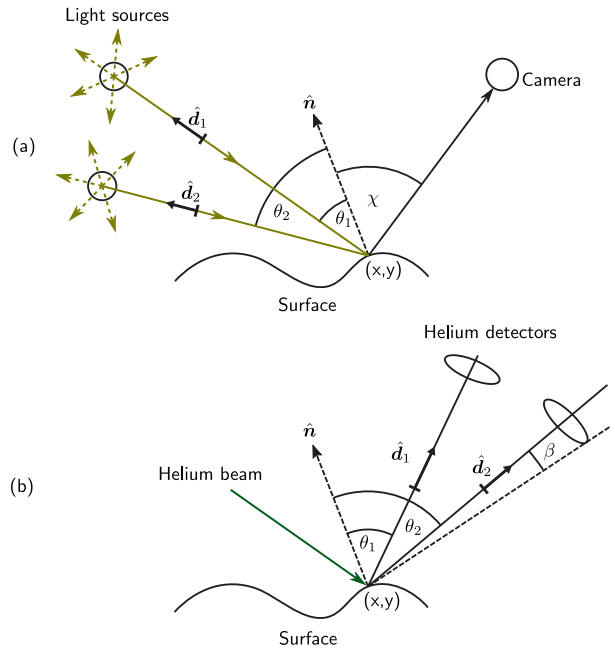

Fig. 13. Correspondence between photometric stereo, (a), and heliometric stereo, (b). $\hat{\boldsymbol{n}}$ is the local unit normal to the surface, $\hat{\boldsymbol{d}}_i$ are the directions to the light sources or detectors. In the case of photography multiple light sources are used to generate images with different $\hat{\boldsymbol{d}}$ vectors, in the case of helium microscopy multiple detectors are used with a single focused illumination to give different $\hat{\boldsymbol{d}}$ by the reciprocity of focused beam imaging.
Source: Figure reproduced from [107].

of particular points of a 2D image when the sample was rotated by a given known angle, so called stereophotogrammetry

To avoid having to map individual sample points in different images, Lambrick and Salvador et al. in 2021 developed a theoretical framework for Heliometric Stereo, an extension of Photometric stereo to helium microscopy [107]. The difference between stereophotogrammetry and photometric stereo is that in photometric stereo the 3D structure is recovered using variations in the intensity signal rather than geometrical displacement of the imaged points. Due to the fact that helium microscopy images are taken in an orthographic projection and constructed by imaging the sample point by point, photometric stereo can be translated to helium in an easy implementation as the image acquisition conditions are highly controlled.

Heliometric stereo is based on the fact that the intensity signal measured in detectors placed in different angles will be different and depend on the tilting angle of the imaged surface (see Fig. 13). This dependency with the scattering distribution is both a curse and a blessing: on the one hand, for heliometric stereo to be implemented straightforwardly one must know the distribution. On the other hand, however, heliometric stereo sets the perfect conditions for estimating this distribution when it is unknown as it samples it for a variety of scattering angles [106,107,134].

8. Conclusion and outlook

In this paper we present an overview of the development of neutral helium atom microscopy (SHeM) from the beginning and up to this day. New developments makes the future look promising: The exciting perspective of true to size 3D imaging, the recent demonstration of sub-resolution contrast which allows fast characterisation of Ångstrom scale roughness over large areas and the improvements in detector technology, just to mention a few. A recent paper shows how the fabrication expenses can be reduced by fabricating some of the complex optical elements required through 3D printing [163].

A range of developments in nanocoatings and micro and nanostructuring applications, including 3d printing down to the micron scale as well as atomic layer advanced manufacturing technology makes the need for a nano-scale stereo characterisation tool evident. This, taken together with the developments in nanocoatings and micro and nanostructuring applications in general, makes it very probable that SHeM will find its use in a larger research and technology community within the next few years. The success of SHeM is likely to depend, at least to some extend, on further investigations of contrast mechanisms. Therefore, the next instrumental development step for SHeM should ideally include the possibility of chopping (pulsing) the beam so that energy resolved measurements (Time of Flight) experiments can be performed. This would allow the different contrast contributions to be separated and analysed independently. It would also enable strategies for reducing the helium background, thus improving the signal to noise ratio which would increase the sensitivity of the instrument. On the other hand, a chopper is difficult to fit into a short beam path as required in microscopes. Maybe the use of a pulsed source can be successfully employed but it has not been tested yet. Chopped beam experiments do however, require fast response time of the detector, which lowers the efficiency.

It would also be interesting to explore contrast mechanisms further in a systematic application of beams of other atoms and helium beams seeded with these other atoms. This would allow for a systematic evaluation of the contrast mechanism according to Eq. (24). For measurements of structures of known composition it may in some cases suffice to characterise the scattering profile independently using HAS on a flat reference surface. All new instruments should be equipped with a simple sample heating, so that water and other contaminates can be removed in order to obtain more contrast information directly from the sample material.

Declaration of competing interest

The authors declare that they have no known competing financial interests or personal relationships that could have appeared to influence the work reported in this paper.

Data availability

No data was used for the research described in the article.

Acknowledgements

We thank William Allison, Paul Dastoor, John Ellis, Daniel Farias, Holly Hedgeland, Andy Jardine, Donald McLaren and Philip Witham for useful discussions and feedback. Furthermore we thank Bruce Doak and Julian Lower with J. Peter Toennies and the Max Plank Society for making Refs. [17,62–65] publicly available for the first time upon our request. GB thanks Giulia Bailo for helpful support. BH acknowledges support of SHeM development from the European Commission through the two collaborative research projects INA, FP6-2003-NEST-A, Grant number 509014 and NEMI, FP7-NMP-2012-SME-6, Grant number 309672.

Appendix A. Simplified model for the pinhole microscope

During the elaboration of this comment we found a simpler solution to the problem of optimising the set up of a pinhole microscope that does not require quadratic expressions.

We can write the following expression for an arbitrary resolution R:

$$R = r_{PH}\sqrt{\psi} + r_S\sqrt{\kappa}. \tag{A.1}$$

Comparing with our FWHM model introduced in [102] we get $\psi = (8/3)\ln(2)(1+\frac{W_D}{a})^2$, $\kappa = 8\ln(2)(\frac{W_D}{a})^2/3$ and R is the FWHM Φ.

This model generalises to other definitions of the resolution R. We note that because the square root is monotonic, we have:

$$max(I) = max(\sqrt{I}) = max(r_{PH} r_S). \tag{A.2}$$

By substitution of Eq. (A.1) into Eq. (A.2) we get:

$$I^* = r_{PH}\left(R - r_{PH}\sqrt{\psi}\right)/\sqrt{\kappa} \tag{A.3}$$

Where we use I^* to indicate that we are dealing with a pseudo intensity that shares its maximum with I. Taking the derivative we get:

$$R - 2r_{PH}\sqrt{\psi} = 0 \leftrightarrow r_{PH}^{opt} = \frac{R}{2\sqrt{\psi}}. \tag{A.4}$$

For our model, $\psi = 8\ln(2)(1+\frac{W_D}{a})^2/3$ and R is the FWHM. Thus, Eq. (26) is recovered.

Appendix B. An overview of published SHeM images and Ph.D. thesis related to SHeM development

Here we present an overview of, to the best of our knowledge, all SHeM images published in the scientific literature so far. The overview is presented as a chronological table (see Table B.1). In addition we present a table of, to the best of our knowledge, all PhD theses related to the topic of SHeM (see Table B.2). We have included links for download where available. Note that master theses and other student reports have not been included. We have cited PhD thesis in the main text in the cases where we have found that they contain relevant work, which has not been published in peer reviewed journals.

Table B.1
Table of SHeM images published in the scientific literature so far.

Ref.	Imaged object	Imaging beam spot size or pinhole diameter
[48]	• hexagonal copper grating (transmission)	3 μm and 2 μm
[51]	• carbon holey foil (Quantifoil®, R2/1) (transmission)	<2 μm and ~2.3 μm
[49]	• carbon holey foil (Quantifoil®, R2/1) (transmission)	<2 μm and ≤1 μm
[2]	• crushed high-field NdFeB magnet • uncoated pollen grain	1.5 μm 1.5 μm
[164]	• aluminium sample • TEM grid, back side, with glass microspheres	
[57]	• uncoated *Crocosmia* pollen grains • debris cluster • silicon wafer	0.35 ± 0.05 μm 0.35 ± 0.05 μm 0.35 ± 0.05 μm
[58]	• Lithium Fluoride (LiF) crystal and LiF debris • IC test pattern, low-k dielectric on Si • crumpled Au film on mica • crumpled mica • line pattern test sample, low-k dielectric on Si • crumpled multilayer graphene • *Crocosmia* pollen grain	0.35 μm 0.35 μm 0.35 μm 0.35 μm 0.35 μm 0.35 μm 0.35 μm
[67]	• broken copper TEM grid • polymer bonded explosives • tin spheres on carbon	5 ± 1 μm 5 ± 1 μm 5 ± 1 μm
[165]	• butterfly wing (*Tirumala hamata*) • TEM grid adhered to Si wafer	pinhole ∅ = 5 μm pinhole ∅ = 5 μm
[166]	• honey bee wing (*Apis mellifera*) • gold logo on Si • gold, nickel, platinum & chromium logo on Si,respectively	5.4 μm 5.4 μm 5.4 μm
[124]	• hexagonal TEM grid suspended off stainless steel • central portion of a silicon nitride x-ray window • sugar crystal (*sucrose*) adhered to a carbon dot • 3D printed step sample, resin (RSF2-GPCL-04) • 3D printed angled planes, resin (RSF2-GPCL-04) • eye of a honey bee (*Apis Melifera*)	$6.9 \pm 0,2$ μm $6.9 \pm 0,2$ μm $6.9 \pm 0,2$ μm $6.9 \pm 0,2$ μm $6.9 \pm 0,2$ μm $6.9 \pm 0,2$ μm
[134]	• TEM grid tick mark	3.5 μm
[162]	• 3D printed sample, resin (RSF2-GPCL-04) • pyrite crystal • trichomes on Mouse-ear Cress (*A. thaliana.*) rosette leaf • dermal denticles on dorsal skin of Port Jackson shark (*Heterodontus portusjacksoni*)	$6.9 \pm 0,2$ μm $6.9 \pm 0,2$ μm $6.9 \pm 0,2$ μm $6.9 \pm 0,2$ μm
[160]	• silicon nitride membrane • australian Emerald Tip Beetle (*Anoplognathus chloropyrus*)	pinhole ∅ = 5 μm pinhole ∅ = 5 μm
[126]	• cleaved LiF crystal	pinhole ∅ = 1.2 μm
[106]	• trenches milled into Si wafer • porous scaffold, Alvetex™ (polystyrene)	pinhole ∅ = 2 μm pinhole ∅ = 2 μm
[69]	• MoS_2 films grown on SiO_2/Si substrate	23 μm
[125]	• thermally evaporated gold films on Si wafer masked by a TEM grid • glass and diamond surfaces for a range of surface finishes • thermally evaporated gold on Si wafers masked by cellulose acetate shadow masks • thermally evaporated gold contacts on Si wafers masked by poly(methyl methacrylate) shadow masks	pinhole ∅ = 5 μm pinhole ∅ = 5 μm pinhole ∅ = 5 μm pinhole ∅ = 5 μm

(*continued on next page*)

(*continued*).

Table B.2
Table of Ph.D. theses related to the topic of SHeM.

Author name	Published, Title, link (if available)
Bodil Holst [167]	1997, University of Cambridge, UK *Atom Optics and Surface Growth Studies using Helium Atom Scattering* ethos.bl.uk/OrderDetails.do?uin=uk.bl.ethos.604194
Stefan Rehbein [54]	2001, Georg-August-University Göttingen, Germany *Entwicklung von freitragenden nanostrukturierten Zonenplatten zur Fokussierung und Monochromatisierung thermischer Helium-Atomstrahlen* cuvillier.de/de/shop/publications/3768
Donald Angus Maclaren [155]	2002, University of Cambridge, UK *Development of a single crystal mirror for scanning helium microscopy* repository.cam.ac.uk/handle/1810/251834

(*continued on next page*)

Table B.2 (*continued*).

Author name	Published, Title, link (if available)
Rob T. Bacon [168]	2007, University of Cambridge, UK *Aspects of atom beam microscopy and scattering from surfaces* ethos.bl.uk/OrderDetails.do?uin=uk.bl.ethos.596236
Ann Elizabeth Weeks [169]	2008, University of Cambridge, UK *Si(111) atom-optical mirrors for scanning helium microscopy* ethos.bl.uk/OrderDetails.do?uin=uk.bl.ethos.611911
Peter Thomas Hustler-Wraight [66]	2008, University of Cambridge, UK *Aspects of atom-surface interactions: considerations for microscopy* ethos.bl.uk/OrderDetails.do?uin=uk.bl.ethos.611936
Kane Michael O'Donnell [170]	2009, University of Newcastle, Australia *Field ionization detection for atom microscopy* hdl.handle.net/1959.13/802939
Andrew Robert Alderwick [139]	2010, University of Cambridge, UK *Instrumental and analysis tools for atom scattering from surfaces* ethos.bl.uk/OrderDetails.do?uin=uk.bl.ethos.608817
Thomas Reisinger [56]	2011, University of Bergen, Norway *Free-standing, axially-symmetric diffraction gratings for neutral matter-waves: experiments and fabrication* bora.uib.no/bora-xmlui/handle/1956/5039
Sabrina Daniela Eder [1]	2012, University of Bergen, Norway *A neutral matter-wave microscope (NEMI): design and setup* bora.uib.no/bora-xmlui/handle/1956/23887
David Matthew Chisnall [171]	2013, University of Cambridge, UK *A high sensitivity detector for helium atom scattering* ethos.bl.uk/OrderDetails.do?uin=uk.bl.ethos.607777
Matthew Gordon Barr [172]	2015, University of Newcastle, Australia *Imaging with atoms: aspects of scanning helium microscopy* http://hdl.handle.net/1959.13/1312654
Gloria Anemone [173]	2017, Universidad Autónoma de Madrid, Spain *Development of Graphene Atomic Mirrors for Neutral Helium Microscopy* repositorio.uam.es/handle/10486/681667
Ranveig Flatabø [174]	2018, University of Bergen, Norway *Charged particle lithography for the fabrication of nanostructured optical elements* bora.uib.no/bora-xmlui/handle/1956/23609
Matthew Bergin [128]	2018, University of Cambridge, UK *Instrumentation and contrast mechanisms in scanning helium microscopy* repository.cam.ac.uk/handle/1810/290645
Adam Joseph Fahy [108]	2018, University of Newcastle, Australia *A practical consideration of scanning helium microscopy* http://hdl.handle.net/1959.13/1397850

(*continued on next page*)

Table B.2 (*continued*).

Author name	Published, Title, link (if available)
Joel Martens [175]	2019, University of Newcastle, Australia *A prototype permanent magnet solenoidal ioniser for the newcastle scanning helium microscope* http://hdl.handle.net/1959.13/1422721
Adrià Salvador Palau [176]	2021, University of Bergen, Norway *On the design of Neutral Scanning Helium Atom Microscopes (SHeM) - Optimal configurations and evaluation of experimental findings* bora.uib.no/bora-xmlui/handle/11250/3009651

References

[1] S.D. Eder, A Neutral Matter-Wave Microscope (NEMI): Design and Setup (Ph.D. thesis), The University of Bergen, 2012, URL https://bora.uib.no/bora-xmlui/handle/1956/23887.

[2] P. Witham, E. Sánchez, A simple approach to neutral atom microscopy, Rev. Sci. Instrum. 82 (10) (2011) 103705, http://dx.doi.org/10.1063/1.3650719.

[3] D.A. MacLaren, W. Allison, Microscopy with atomic beams: contrast in a scanning helium microscope, Inst. Phys. Conf. Ser. 179 (2004) 383–388.

[4] A.S. Palau, SHeM: Utilities for Scanning Helium Microscopy, Molecular beams, and supersonic expansions into vacuum, 2021, https://github.com/envitricollat/SHeM.

[5] S. Lambrick, D. Seremet, SHeM-Ray-Tracing-Simulation: A ray tracing simulation of the Cambridge SHeM sample chamber used for predicting contrast in images, 2018, https://github.com/slambrick/SHeM-Ray-Tracing-Simulation.

[6] I. Estermann, O. Stern, Beugung von Molekularstrahlen, Z. Physik 61 (1) (1930) 95–125, http://dx.doi.org/10.1007/BF01340293.

[7] H. Pauly, Atom, Molecule, and Cluster Beams I: Basic Theory, Production and Detection of Thermal Energy Beams, Vol. 28, Springer Science & Business Media, 2000.

[8] A. Kantrowitz, J. Grey, A High Intensity Source for the Molecular Beam. Part I. Theoretical, Rev. Sci. Instrum. 22 (5) (1951) 328–332, http://dx.doi.org/10.1063/1.1745921.

[9] G. Brusdeylins, R.B. Doak, J.P. Toennies, Measurement of the Dispersion Relation for Rayleigh Surface Phonons of LiF(001) by Inelastic Scattering of He Atoms, Phys. Rev. Lett. 46 (6) (1981) 437–439, http://dx.doi.org/10.1103/PhysRevLett.46.437.

[10] G. Benedek, J.P. Toennies, Atomic Scale Dynamics at Surfaces: Theory and Experimental Studies with Helium Atom Scattering, Vol. 63, Springer, Berlin/Heidelberg, 2018.

[11] B. Holst, G. Alexandrowicz, N. Avidor, G. Benedek, G. Bracco, W.E. Ernst, D. Farías, A.P. Jardine, K. Lefmann, J.R. Manson, R. Marquardt, S.M. Artés, S.J. Sibener, J.W. Wells, A. Tamtögl, W. Allison, Material properties particularly suited to be measured with helium scattering: selected examples from 2D materials, van der Waals heterostructures, glassy materials, catalytic substrates, topological insulators and superconducting radio frequency materials, Phys. Chem. Chem. Phys. 23 (2021) 7653–7672, http://dx.doi.org/10.1039/D0CP05833E.

[12] B. Holst, G. Bracco, Surface Science Techniques, in: Springer Series in Surface Sciences, Vol. 51, Springer, 2013, pp. 333–367 (Chapter 12) Probing Surfaces with Thermal He Atoms: Scattering and Microsocpy with a Soft Touch.

[13] D. Farías, K.-H. Rieder, Atomic beam diffraction from solid surfaces, Rep. Progr. Phys. 61 (12) (1998) 1575–1664, http://dx.doi.org/10.1088/0034-4885/61/12/001.

[14] R.B. Doak, Focusing of a helium atom beam, in: Optical Society of America Annual Meeting Technical Digest, 1990, p. 250, http://dx.doi.org/10.1364/OAM.1990.FR2.

[15] R.B. Doak, Focusing of an atomic helium beam using bent crystal reflecting optics, Bull. Am. Phys. Soc. (1990) 645.

[16] R.B. Doak, Experimental limitations and opportunities in single-phonon inelastic helium scattering, in: E. Hulpke (Ed.), Helium Atom Scattering from Surfaces. Springer Series in Surface Sciences, Vol. 27, Springer Berlin Heidelberg, 1992, pp. 5–24, http://dx.doi.org/10.1007/978-3-662-02774-5_2.

[17] R.B. Doak, Focusing of an Atomic Beam, 2022/1989, https://arxiv.org/abs/2201.06201.

[18] O. Carnal, M. Sigel, T. Sleator, H. Takuma, J. Mlynek, Imaging and Focusing of Atoms by a Fresnel Zone Plate, Phys. Rev. Lett. 67 (23) (1991) 3231–3234, http://dx.doi.org/10.1103/PhysRevLett.67.3231.

[19] B. Holst, W. Allison, An atom-focusing mirror, Nature 390 (6657) (1997) 244, http://dx.doi.org/10.1038/36769.

[20] B. Holst, W. Allison, Focusing helium atom beams using single crystal surfaces, in: Roger Campargue (Ed.), Atomic and Molecular Beams: The State of the Art 2000, Springer Berlin Heidelberg, 2001, pp. 183–194.

[21] B. Holst, J.R. Buckland, W. Allison, Spatial mapping in the electron-impact ion-source of a residual gas analyser, Vacuum 53 (1) (1999) 207–210, http://dx.doi.org/10.1016/S0042-207X(98)00388-1.

[22] R.B. Doak, R.E. Grisenti, S. Rehbein, G. Schmahl, J.P. Toennies, Ch. Wöll, Towards Realization of an Atomic de Broglie Microscope: Helium Atom Focusing Using Fresnel Zone Plates, Phys. Rev. Lett. 83 (21) (1999) 4229–4232, http://dx.doi.org/10.1103/PhysRevLett.83.4229.

[23] R.J. Wilson, B. Holst, W. Allison, Optical properties of mirrors for focusing of non-normal incidence atom beams, Rev. Sci. Instrum. 70 (7) (1999) 2960–2967, http://dx.doi.org/10.1063/1.1149854.

[24] D.A. MacLaren, W. Allison, B. Holst, Single crystal optic elements for helium atom microscopy, Rev. Sci. Instrum. 71 (7) (2000) 2625–2634, http://dx.doi.org/10.1063/1.1150667.

[25] D.A. MacLaren, H.T. Goldrein, B. Holst, W. Allison, Phase-stepping optical profilometry of atom mirrors, J. Phys. D: App. Phys. 36 (15) (2003) 1842–1849, http://dx.doi.org/10.1088/0022-3727/36/15/315.

[26] B. Holst, J.M. Huntley, R. Balsod, W. Allison, Mechanical properties of ultra-thin single crystals for atom-mirror applications: Au(001), Si(001), J. Phys. D: Appl. Phys. 32 (20) (1999) 2666–2673, http://dx.doi.org/10.1088/0022-3727/32/20/313.

[27] K. Fladischer, H. Reingruber, T. Reisinger, V. Mayrhofer, W.E. Ernst, A.E. Ross, D.A. MacLaren, W. Allison, D. Litwin, J. Galas, S. Sitarek, P. Nieto, D. Barredo, D. Farías, R. Miranda, B. Surma, A. Miros, B. Piatkowski, E. Søndergård, B. Holst, An ellipsoidal mirror for focusing neutral atomic and molecular beams, New J. Phys. 12 (3) (2010) 033018, http://dx.doi.org/10.1088/1367-2630/12/3/033018.

[28] D.A. MacLaren, N.J. Curson, P. Atkinson, W. Allison, An AFM study of the processing of hydrogen passivated silicon(111) of a low miscut angle, Surf. Sci. 490 (3) (2001) 285–295, http://dx.doi.org/10.1016/S0039-6028(01)01331-0.

[29] D.A. MacLaren, N.J. Curson, P. Atkinson, B. Holst, D.J. Johnson, W. Allison, Simple design for the transportation of *ex situ* prepared hydrogen passivated silicon, J. Vac. Sci. Technol. A 20 (2002) 285–287, http://dx.doi.org/10.1116/1.1419084.

[30] D. Barredo, F. Calleja, A.E. Weeks, P. Nieto, J.J. Hinarejos, G. Laurent, A.L. Vazquez de Parga, D.A. MacLaren, D. Farias, W. Allison, R. Miranda, Si(111)-H(1x1): A mirror for atoms characterized by AFM, STM, He and H_2 diffraction, Surf. Sci. 601 (1) (2007) 24–29, http://dx.doi.org/10.1016/j.susc.2006.08.048.

[31] J.R. Buckland, W. Allison, Determination of the helium/Si(111)-(1x1)H potential, J. Chem. Phys. 112 (2) (2000) 970–978, http://dx.doi.org/10.1063/1.480723.

[32] J.R. Buckland, B. Holst, W. Allison, Helium reflectivity of the Si(111)-(1x1)H surface for use in atom optical elements, Chem. Phys. Lett. 303 (1) (1999) 107–110, http://dx.doi.org/10.1016/S0009-2614(99)00182-7.

[33] D. Barredo, F. Calleja, P. Nieto, J.J. Hinarejos, G. Laurent, A.L.V. de Parga, D. Farías, R. Miranda, A Quantum-Stabilized Mirror for Atoms, Adv. Mater. 20 (18) (2008) 3492–3497, http://dx.doi.org/10.1002/adma.200800866.

[34] G. Anemone, A. Al Taleb, S.D. Eder, B. Holst, D. Farías, Flexible thin metal crystals as focusing mirrors for neutral atomic beams, Phys. Rev. B 95 (20) (2017) 205428, http://dx.doi.org/10.1103/PhysRevB.95.205428.

[35] D. Litwin, J. Galas, T. Kozlowski, S. Sitarek, Measurements of the geometrical characteristics of the silicon wafer for helium microscope focusing mirror, in: R.S. Romaniuk, S. Simrock, V.M. Lutkovski (Eds.), Photonics Applications in Industry and Research IV, Vol. 5948, International Society for Optics and Photonics, SPIE, 2005, pp. 177–184, http://dx.doi.org/10.1117/12.622456.

[36] A.E. Weeks, D. Litwin, J. Galas, B. Surma, B. Piatkowski, D.A. MacLaren, W. Allison, Accurate surface profilometry of ultrathin wafers, Semicond. Sci. Technol. 22 (9) (2007) 997–1002, http://dx.doi.org/10.1088/0268-1242/22/9/004.

[37] D. Litwin, J. Galas, S. Sitarek, B. Surma, B. Piatkowski, A. Miros, Temperature influence in confocal techniques for a silicon wafer testing, in: F. Baldini, J. Homola, R.A. Lieberman, M. Miler (Eds.), Optical Sensing Technology and Applications, Vol. 6585, International Society for Optics and Photonics, SPIE, 2007, pp. 247–254, http://dx.doi.org/10.1117/12.722850.

[38] J. Galas, D. Litwin, S. Sitarek, B. Surma, B. Piatkowski, Symmetry descriptors for Si wafer characterisation for scanning helium atomic beam microscopy mirror, in: G. Cheriaux, C.J. Hooker, M. Stupka (Eds.), Adaptive Optics for Laser Systems and Other Applications, Vol. 6584, International Society for Optics and Photonics, SPIE, 2007, pp. 95–100, http://dx.doi.org/10.1117/12.722841.

[39] K. Fladischer, D. Litwin, J. Galas, A.E. Weeks, D.A. MacLaren, R. Lammegger, H. Sormann, W.E. Ernst, B. Holst, An optical profilometer for characterizing complex surfaces under high vacuum conditions, Precis. Eng. 32 (3) (2008) 182–185, http://dx.doi.org/10.1016/j.precisioneng.2007.08.001.

[40] D. Litwin, J. Galas, S. Sitarek, B. Surma, B. Piatkowski, Chromatic sensor-based-profilometer for the focusing mirror in the Scanning Helium Microscope, in: A. Popiolek-Masajada, E. Jankowska, W. Urbanczyk (Eds.), 16th Polish-Slovak-Czech Optical Conference on Wave and Quantum Aspects of Contemporary Optics, Vol. 7141, International Society for Optics and Photonics, SPIE, 2008, pp. 483–489, http://dx.doi.org/10.1117/12.822411.

[41] J. Sass, K. Mazur, B. Surma, F. Eichhorn, D. Litwin, J. Galas, S. Sitarek, X-ray studies of ultra-thin Si wafers for mirror application, Nucl. Instrum. Methods Phys. Res. B 253 (1) (2006) 236–240, http://dx.doi.org/10.1016/j.nimb.2006.10.057.

[42] W. Allison A. E. Ross, Finite element analysis of adaptive atom-optical mirrors, J. Phys. D: Appl. Phys. 44 (18) (2011) 185501, http://dx.doi.org/10.1088/0022-3727/44/18/185501.

[43] H.C. Schewe, B.S. Zhao, G. Meijer, W. Schöllkopf, Focusing a helium atom beam using a quantum-reflection mirror, New J. Phys. 11 (11) (2009) 113030, http://dx.doi.org/10.1088/1367-2630/11/11/113030.

[44] B.S. Zhao, H.C. Schewe, G. Meijer, W. Schöllkopf, Coherent Reflection of He Atom Beams from Rough Surfaces at Grazing Incidence, Phys. Rev. Lett. 105 (2010) 133203, http://dx.doi.org/10.1103/PhysRevLett.105.133203.

[45] P. Sutter, M. Minniti, P. Albrecht, D. Farías, R. Miranda, E. Sutter, A high-reflectivity, ambient-stable graphene mirror for neutral atomic and molecular beams, Appl. Phys. Lett. 99 (21) (2011) 211907, http://dx.doi.org/10.1063/1.3663866.

[46] E. Sutter, P Albrecht, F.E. Camino, P. Sutter, Monolayer graphene as ultimate chemical passivation layer for arbitrarily shaped metal surfaces, Carbon 48 (15) (2010) 4414–4420, http://dx.doi.org/10.1016/j.carbon.2010.07.058.

[47] G. Anemone, C. Weingarten, A. Al Taleb, C. Prieto, D. Farías, Ultrasmooth metal thin films on curved fused silica by laser polishing, Appl. Phys. Lett. 111 (18) (2017) 181602, http://dx.doi.org/10.1063/1.4999917.

[48] M. Koch, S. Rehbein, G. Schmahl, T. Reisinger, G. Bracco, W.E. Ernst, B. Holst, Imaging with neutral atoms - a new matter-wave microscope, J. Microsc. 229 (1) (2008) 1–5, http://dx.doi.org/10.1111/j.1365-2818.2007.01874.x.

[49] S.D. Eder, T. Reisinger, M.M. Greve, G. Bracco, B. Holst, Focusing of a neutral helium beam below one micron, New J. Phys. 14 (7) (2012) 073014, http://dx.doi.org/10.1088/1367-2630/14/7/073014.

[50] S.D. Eder, A.K. Ravn, B. Samelin, G. Bracco, A.S. Palau, T. Reisinger, E.B. Knudsen, K. Lefmann, B. Holst, Zero-order filter for diffractive focusing of de Broglie matter waves, Phys. Rev. A 95 (2) (2017) 023618, http://dx.doi.org/10.1103/PhysRevA.95.023618.

[51] T. Reisinger, B. Holst, Neutral atom and molecule focusing using a Fresnel zone plate, J. Vac. Sci. Technol. B 26 (6) (2008) 2374–2379, http://dx.doi.org/10.1116/1.2987955.

[52] T. Reisinger, M.M. Greve, S.D. Eder, G. Bracco, B. Holst, Brightness and virtual source size of a supersonic deuterium beam, Phys. Rev. A 86 (4) (2012) 043804, http://dx.doi.org/10.1103/PhysRevA.86.043804.

[53] S. Rehbein, Nanofabrication of diffractive optics for soft X-ray and atom beam focusing, J. Phys. IV France 104 (2003) 207–210.

[54] S. Rehbein, Entwicklung von freitragenden nanostrukturierten Zonenplatten zur Fokussierung und Monochromatisierung thermischer Helium-Atomstrahlen (Ph.D. thesis), University of Göttingen, 2001, URL https://cuvillier.de/de/shop/publications/3768.

[55] T. Reisinger, S. Eder, M.M. Greve, H.I. Smith, B. Holst, Free-standing silicon-nitride zoneplates for neutral-helium microscopy, Microelectron. Eng. 87 (5) (2010) 1011–1014, http://dx.doi.org/10.1016/j.mee.2009.11.107.

[56] T. Reisinger, Free-standing, axially-symmetric diffraction gratings for neutral matter-waves: experiments and fabrication (Ph.D. thesis), University of Bergen, 2011, URL https://bora.uib.no/bora-xmlui/handle/1956/5039.

[57] P.J. Witham, E. Sánchez, Increased resolution in neutral atom microscopy, J. Microsc. 248 (3) (2012) 223–227, http://dx.doi.org/10.1111/j.1365-2818.2012.03665.x.

[58] P. Witham, E. Sánchez, Exploring neutral atom microscopy, Cryst. Res. Technol. 49 (9) (2014) 690–698, http://dx.doi.org/10.1002/crat.201300401.

[59] P.J. Witham, Neutral Atom Microscopy (Master's thesis), Portland State University, 2013, URL https://pdxscholar.library.pdx.edu/open_access_etds/1407/.

[60] M. Barr, K.M. O'Donnell, A. Fahy, W. Allison, P.C. Dastoor, A desktop supersonic free-jet beam source for a scanning helium microscope (SHeM), Meas. Sci. Technol. 23 (10) (2012) 105901, http://dx.doi.org/10.1088/0957-0233/23/10/105901.

[61] John Ellis, Private communication, 2022.

[62] J.C.A. Lower, The helium atom microscope - report 1, 2022/1992, http://hdl.handle.net/21.11116/0000-0009-FA5D-6.

[63] J.C.A. Lower, Count rate and the helium atom microscope - report 2, 2022/1992, http://hdl.handle.net/21.11116/0000-0009-FA65-C.

[64] J.C.A. Lower, The helium atom microscope - report 3, 2022/1992, http://hdl.handle.net/21.11116/0000-0009-FA6A-7.

[65] J.C.A. Lower, Coherence length, coherence width and the helium atom microscope, 2022/1992, http://hdl.handle.net/21.11116/0000-0009-FA74-B.

[66] P.T. Hustler-Wraight, Aspects of Atom-Surface Interactions: Considerations for Microscopy (Ph.D. thesis), University of Cambridge, 2008.

[67] M. Barr, A. Fahy, A. Jardine, J. Ellis, D. Ward, D.A. MacLaren, W. Allison, P.C. Dastoor, A design for a pinhole scanning helium microscope, Nucl. Instrum. Methods Phys. Res. B 340 (2014) 76–80, http://dx.doi.org/10.1016/j.nimb.2014.06.028.

[68] A.S. Palau, S.D. Eder, T. Andersen, A.K. Ravn, G. Bracco, B. Holst, Center-line intensity of a supersonic helium beam, Phys. Rev. A 98 (6) (2018) 063611, http://dx.doi.org/10.1103/PhysRevA.98.063611.

[69] G. Bhardwaj, K.R. Sahoo, R. Sharma, P. Nath, P.R. Shirhatti, Neutral-atom-scattering-based mapping of atomically thin layers, Phys. Rev. A 105 (2022) 022828, http://dx.doi.org/10.1103/PhysRevA.105.022828.

[70] S.D. Eder, A. Salvador Palau, T. Kaltenbacher, G. Bracco, B. Holst, Velocity distributions in microskimmer supersonic expansion helium beams: High precision measurements and modeling, Rev. Sci. Instrum. 89 (11) (2018) 113301, http://dx.doi.org/10.1063/1.5044203.

[71] H.C.W. Beijerinck, N.F. Verster, Absolute intensities and perpendicular temperatures of supersonic beams of polyatomic gases, Physica B+C 111 (2–3) (1981) 327–352, http://dx.doi.org/10.1016/0378-4363(81)90112-1.

[72] J. Braun, P.K. Day, J.P. Toennies, G. Witte, E. Neher, Micrometer-sized nozzles and skimmers for the production of supersonic He atom beams, Rev. Sci. Instrum. 68 (8) (1997) 3001–3009, http://dx.doi.org/10.1063/1.1148233.

[73] D.P. DePonte, S.D. Kevan, F. Patton, Brightness of micronozzle helium source, Rev. Sci. Instrum. 77 (5) (2006) 055107, http://dx.doi.org/10.1063/1.2198813.

[74] H. Hedgeland, A.P. Jardine, W. Allison, J. Ellis, Anomalous attenuation at low temperatures in high-intensity helium beam sources, Rev. Sci. Instrum. 76 (12) (2005) 123111, http://dx.doi.org/10.1063/1.2149008.

[75] U. Even, The even-lavie valve as a source for high intensity supersonic beam, EPJ Tech. Instrum. 2 (17) (2015) http://dx.doi.org/10.1140/epjti/s40485-015-0027-5.

[76] Y. Segev, N. Bibelnik, N. Akerman, Y. Shagam, A. Luski, M. Karpov, J. Narevicius, E. Narevicius, Molecular beam brightening by shock-wave suppression, Sci. Adv. 3 (2017) e1602258, http://dx.doi.org/10.1126/sciadv.1602258.

[77] D.R. Miller, Free jet sources, in: G. Scoles (Ed.), Atomic and Molecular Beam Methods: 1, Oxford University Press, Oxford, New York, 1988, pp. 14–53 (Chapter 2).

[78] G.S. Sikora, Analysis of Asymptotic Behavior of Free-Jets: Prediction of Molecular Beam Intensity and Velocity Distributions (Ph.D. thesis), Princeton University, 1974, URL https://www.proquest.com/docview/302656620?pq-origsite=gscholar&fromopenview=true.

[79] U. Bossel, Skimming of molecular beams from diverging non-equilibrium gas jets, in: Presented at the 11th Bien. Fluid Dyn. Symp. on Advanced Probl. and Method in Fluid Mech, 1974, pp. 3–8.

[80] G.A. Bird, Molecular Gas Dynamics and the Direct Simulation of Gas Flows, Clarendon Press, Oxford, 1994.

[81] G.A. Bird, Direct simulation and the Boltzmann equation, Phys. Fluids 13 (11) (1970) 2676–2681, http://dx.doi.org/10.1063/1.1692849.

[82] G.A. Bird, Transition regime behavior of supersonic beam skimmers, Phys. Fluids 19 (10) (1976) 1486–1491, http://dx.doi.org/10.1063/1.861351.

[83] M.J. Verheijen, H.C.W. Beijerinck, W.A. Renes, N.F. Verster, A quantitative description of skimmer interaction in supersonic secondary beams: Calibration of absolute intensities, Chem. Phys. 85 (1) (1984) 63–71, http://dx.doi.org/10.1016/S0301-0104(84)85173-3.

[84] H. Ashkenas, F.S. Sherman, The structure and utilization of supersonic free jets in low density wind tunnels, in: Proceedings of the 4th International Symposium on Rarefied Gas Dynamics, 1966, pp. 84–105.

[85] B.B. Hamel, D.R. Willis, Kinetic theory of source flow expansion with application to the free jet, Phys. Fluids 9 (5) (1966) 829–841, http://dx.doi.org/10.1063/1.1761783.

[86] R.E. Grundy, Axially symmetric expansion of a monatomic gas from an orifice into a vacuum, Phys. Fluids 12 (10) (1969) 2011–2018, http://dx.doi.org/10.1063/1.1692306.

[87] J.E. Jones, On the determination of molecular fields.—I. From the variation of the viscosity of a gas with temperature, Proc. R. Soc. A 106 (738) (1924) 441–462, http://dx.doi.org/10.1098/rspa.1924.0081.

[88] K.T. Tang, J.P. Toennies, C.L. Yiu, Accurate analytical He-He van der Waals potential based on perturbation theory, Phys. Rev. Lett. 74 (9) (1995) 1546–1549, http://dx.doi.org/10.1103/PhysRevLett.74.1546.

[89] J.J. Hurly, M.R. Moldover, Ab initio values of the thermophysical properties of helium as standards, J. Res. Natl. Inst. Stand. Technol. 105 (5) (2000) 667–688, http://dx.doi.org/10.6028/jres.105.054.

[90] L. Pedemonte, G. Bracco, R. Tatarek, Theoretical and experimental study of He free-jet expansions, Phys. Rev. A 59 (4) (1999) 3084–3087, http://dx.doi.org/10.1103/PhysRevA.59.3084.

[91] L. Pedemonte, G. Bracco, Study of He flow properties to test He dimer potentials, J. Chem. Phys. 119 (3) (2003) 1433–1441, http://dx.doi.org/10.1063/1.1580801.

[92] T. Reisinger, G. Bracco, S. Rehbein, G. Schmahl, W.E. Ernst, B. Holst, Direct images of the virtual source in a supersonic expansion, J. Phys. Chem. A 111 (49) (2007) 12620–12628, http://dx.doi.org/10.1021/jp076102u.

[93] K. Nanbu, Variable hard-sphere model for gas mixture, J. Phys. Soc. Japan 59 (12) (1990) 4331–4333, http://dx.doi.org/10.1143/JPSJ.59.4331.

[94] G.A. Bird, Recent advances and current challenges for DSMC, Comput. Math. Appl. 35 (1–2) (1998) 1–14, http://dx.doi.org/10.1016/S0898-1221(97)00254-X.

[95] K. Luria, W. Christen, U. Even, Generation and propagation of intense supersonic beams, J. Phys. Chem. A 115 (25) (2011) 7362–7367, http://dx.doi.org/10.1021/jp201342u.

[96] G. Markelov, M. Ivanov, A comparative analysis of 2D/3D micronozzle flows by the DSMC method, in: 39th Aerospace Sciences Meeting and Exhibit, 2001, pp. 1–13, http://dx.doi.org/10.2514/6.2001-1009.

[97] A. Salvador Palau, G. Bracco, B. Holst, Theoretical model of the helium zone plate microscope, Phys. Rev. A 95 (1) (2017) 13611, http://dx.doi.org/10.1103/PhysRevA.95.013611.

[98] A.H.M. Habets, Upersonic Expansion of Argon into Vacuum (Ph.D. thesis), Technische Hogeschool Eindhoven, 1977, URL https://inis.iaea.org/collection/NCLCollectionStore/_Public/08/302/8302199.pdf.

[99] A. Amirav, U. Even, J. Jortner, Cooling of large and heavy molecules in seeded supersonic beams, Chem. Phys. 51 (1–2) (1980) 31–42, http://dx.doi.org/10.1016/0301-0104(80)80077-2.

[100] J.P. Toennies, K. Winkelmann, Theoretical studies of highly expanded free jets: Influence of quantum effects and a realistic intermolecular potential, J. Chem. Phys. 66 (9) (1977) 3965–3979, http://dx.doi.org/10.1063/1.434448.

[101] S.D. Eder, G. Bracco, T. Kaltenbacher, B. Holst, Two dimensional imaging of the virtual source of a supersonic beam: helium at 125 K, J. Phys. Chem. A 118 (2013) 4–12, http://dx.doi.org/10.1021/jp4082855.

[102] A.S. Palau, G. Bracco, B. Holst, Theoretical model of the helium pinhole microscope, Phys. Rev. A 94 (6) (2016) 063624, http://dx.doi.org/10.1103/PhysRevA.94.063624.

[103] T. Kaltenbacher, Optimization of a constrained linear monochromator design for neutral atom beams, Ultramicroscopy 163 (2016) 62–68, http://dx.doi.org/10.1016/j.ultramic.2016.02.003.

[104] M. Bergin, D.J. Ward, J. Ellis, A.P. Jardine, A method for constrained optimisation of the design of a scanning helium microscope, Ultramicroscopy 207 (2019) 112833, http://dx.doi.org/10.1016/j.ultramic.2019.112833.

[105] D.C. Joy, R. Ramachandra, B.J. Griffin, Choosing a beam-electrons, protons, He or Ga ions? Microsc. Microanal. 15 (2009) http://dx.doi.org/10.1017/S1431927609092757.

[106] S.M. Lambrick, L. Vozdecky, M. Bergin, J.E. Halpin, D.A. MacLaren, P.C. Dastoor, S.A. Przyborski, A.P. Jardine, D.J. Ward, Multiple scattering in scanning helium microscopy, Appl. Phys. Lett. 116 (6) (2020) 061601, http://dx.doi.org/10.1063/1.5143950.

[107] S.M. Lambrick, A.S. Palau, P.E. Hansen, G. Bracco, J. Ellis, A.P. Jardine, B. Holst, True-to-size surface mapping with neutral helium atoms, Phys. Rev. A 103 (5) (2021) 053315, http://dx.doi.org/10.1103/PhysRevA.103.053315.

[108] A.J. Fahy, Practical Consideration of Scanning Helium Microscopy (Ph.D. thesis), University of Newcastle, 2019, URL https://nova.newcastle.edu.au/vital/access/manager/Repository/uon:34367.

[109] A.G. Michette, Optical Systems for Soft X Rays, Plenum Press, New York, London, 1986.

[110] R. Flatabø, S.D. Eder, A.K. Ravn, B. Samelin, M.M. Greve, T. Reisinger, B. Holst, Fast resolution change in neutral helium atom microscopy, Rev. Sci. Instrum. 89 (5) (2018) 053702, http://dx.doi.org/10.1063/1.5029385.

[111] T.S. McKechnie, General Theory of Light Propagation and Imaging Through the Atmosphere, Springer, 2016.

[112] L. Kipp, M. Skibowski, R.L. Johnson, R. Berndt, R. Adelung, S. Harm, R. Seemann, Sharper images by focusing soft X-rays with photon sieves, Nature 414 (6860) (2001) 184–188, http://dx.doi.org/10.1038/35102526.

[113] S.D. Eder, X. Guo, T. Kaltenbacher, M.M. Greve, M. Kalläne, L. Kipp, B. Holst, Focusing of a neutral helium beam with a photon-sieve structure, Phys. Rev. A 91 (4) (2015) 043608, http://dx.doi.org/10.1103/PhysRevA.91.043608.

[114] R. Flatabø, M.M. Greve, S.D. Eder, M. Kalläne, A.S. Palau, K.K. Berggren, B. Holst, Atom sieve for nanometer resolution neutral helium microscopy, J. Vac. Sci. Technol. B 35 (6) (2017) 06G502, http://dx.doi.org/10.1116/1.4994330.

[115] M.M. Greve, A.M. Vial, J.J. Stamnes, B. Holst, The Beynon Gabor zone plate: A new tool for de Broglie matter waves and hard X-rays? An off axis and focus intensity investigation, Opt. Express 21 (2013) 28483–28495, http://dx.doi.org/10.1364/OE.21.028483.

[116] M. Bergin, W. Roland-Batty, C.J. Hatchwell, T.A. Myles, J. Martens, A. Fahy, M. Barr, W.J. Belcher, P.C. Dastoor, Standardizing resolution definition in scanning helium microscopy, Ultramicroscopy (2021) 113453, http://dx.doi.org/10.1016/j.ultramic.2021.113453.

[117] A.R. Alderwick, A.P. Jardine, W. Allison, J. Ellis, An evaluation of the kinematic approximation in helium atom scattering using wavepacket calculations, Surf. Sci. 678 (2018) 65–71, http://dx.doi.org/10.1016/j.susc.2018.04.019.

[118] B. Poelsema, L.K. Verheij, G. Comsa, Direct evidence for two-dimensional Xe gas-solid phase transition on Pt(111) by means of thermal He scattering, Phys. Rev. Lett. 51 (1983) 2410–2413, http://dx.doi.org/10.1103/PhysRevLett.51.2410.

[119] A.M. Lahee, J.R. Manson, J.P. Toennies, C. Wöll, Observation of interference oscillations in helium scattering from single surface defects, Phys. Rev. Lett. 57 (1986) 471–474, http://dx.doi.org/10.1103/PhysRevLett.57.471.

[120] B. Poelsema, K. Lenz, L.S. Brown, L.K. Verheij, G. Comsa, Lateral distribution of ion bombardment induced defects on Pt(111) at 80 K, Surf. Sci. 162 (1) (1985) 1011–1016, http://dx.doi.org/10.1016/0039-6028(85)91015-5.

[121] P. Kraus, C. Gösweiner, A. Tamtögl, F. Apolloner, W.E. Ernst, Adhesion properties of hydrogen on Sb(111) probed by helium atom scattering, Europhys. Lett 114 (5) (2016) 56001, http://dx.doi.org/10.1209/0295-5075/114/56001.

[122] B. Poelsema, G. Comsa, The Scattering Mechanism, Springer Berlin Heidelberg, Berlin, Heidelberg, 1989, http://dx.doi.org/10.1007/BFb0045232.

[123] E. Mete, I. Demiroğlu, E. Albayrak, G. Bracco, S. Ellialtioğlu, M.F. Danişman, Influence of steps on the tilting and adsorption dynamics of ordered pentacene films on vicinal Ag(111) surfaces, J. Phys. Chem. C 116 (36) (2012) 19429–19433, http://dx.doi.org/10.1021/jp306463w.

[124] A. Fahy, S.D. Eder, M. Barr, J. Martens, T.A. Myles, P.C. Dastoor, Image formation in the scanning helium microscope, Ultramicroscopy 192 (2018) 7–13, http://dx.doi.org/10.1016/j.ultramic.2018.05.004.

[125] S.D. Eder, A. Fahy, M.G. Barr, J. Manson, B. Holst, P.C. Dastoor, Sub-resolution contrast in neutral helium microscopy through factet scattering for quantitative imaging of nanoscale topographies on macroscopic surface, Nature Commun. 14 (2023) 904, http://dx.doi.org/10.1038/s41467-023-36578-x.

[126] M. Bergin, S.M. Lambrick, H. Sleath, D.J. Ward, J. Ellis, A.P. Jardine, Observation of diffraction contrast in scanning helium microscopy, Sci. Rep. 10 (1) (2020) 1–8, http://dx.doi.org/10.1038/s41598-020-58704-1.

[127] M. Barr, A. Fahy, J. Martens, A.P. Jardine, D.J. Ward, J. Ellis, W. Allison, P.C. Dastoor, Unlocking new contrast in a scanning helium microscope, Nature Commun. 7 (2016) 10189, http://dx.doi.org/10.1038/ncomms10189.

[128] M. Bergin, Nstrumentation and Contrast Mechanisms in Scanning Helium Microscopy (Ph.D. thesis), University of Cambridge, 2019, URL https://www.repository.cam.ac.uk/handle/1810/290645.

[129] V.M. Torres, M. Stevens, J.L. Edwards, D.J. Smith, R.B. Doak, I.S.T. Tsong, Growth of AlN and GaN on 6H–SiC(0001) using a helium supersonic beam seeded with ammonia, Appl. Phys. Lett. vol. 71 (10) (1997) 1365–1367, http://dx.doi.org/10.1063/1.119895.

[130] J. Greenwood, The correct and incorrect generation of a cosine distribution of scattered particles for Monte-Carlo modelling of vacuum systems, Vacuum 67 (2002) 217, http://dx.doi.org/10.1016/S0042-207X(02)00173-2.

[131] D.R. O'Keefe, R.L. Palmer, Atomic and molecular beam scattering from macroscopically rough surfaces, J. Vac. Sci. Technol. 8 (2001) 27–30, http://dx.doi.org/10.1116/1.1492975.

[132] E.P. Wenaas, Equilibrium cosine law and scattering symmetry at the gas–surface interface, J. Chem. Phys. 54 (1) (1971) 376–388, http://dx.doi.org/10.1063/1.1674619.

[133] R. Feres, G. Yablonsky, Knudsen's cosine law and random billiards, Chem. Eng. Sci. 59 (7) (2004) 1541–1556, http://dx.doi.org/10.1016/j.ces.2004.01.016.

[134] S.M. Lambrick, M. Bergin, A.P. Jardine, D.J. Ward, A ray tracing method for predicting contrast in neutral atom beam imaging, Micron 113 (2018) 61–68, http://dx.doi.org/10.1016/j.micron.2018.06.014.

[135] S.M. Lambrick, M. Bergin, D.J. Ward, M. Barr, A. Fahy, T. Myles, A. Radic, P.C. Dastoor, J. Ellis, A.P. Jardine, Observation of diffuse scattering in scanning helium microsocpy, Phys. Chem. Chem. Phys. 24 (2022) 26539, http://dx.doi.org/10.1039/D2CP01951E.

[136] B. Samelin, Neu- und weiterentwicklung von Elektronensto≃-ionisationsdetektoren (Master's thesis), Max Planck Institute for Fluid dynamics, Göttingen, 1993.

[137] H. Hedgeland, The Development of Quasi-Elastic Helium-3 Spin-Echo Spectroscopy as a Tool for the Study of Surface Dynamics (Ph.D. thesis), University of Cambridge, 2007, https://ethos.bl.uk/OrderDetails.do?uin=uk.bl.ethos.603936.

[138] E. Keppler, V. Afonin, C. Curtis, A. Dyachkov, J. Erö, C. Fan, K. Hsieh, D. Hunten, W.-H. Ip, A. Richter, et al., Neutral gas measurements of comet Halley from Vega 1, Nature 321 (6067) (1986) 273–274.

[139] A.R. Alderwick, Nstrumental and Analysis Tools for Atom Scattering from Surfaces (Ph.D. Thesis), University of Cambridge, 2010, URL https://ethos.bl.uk/OrderDetails.do?uin=uk.bl.ethos.608817.

[140] H.G. Bullman, Development of a Position Sensitive Atom Detector for Helium-Surface Scattering (Ph.D. thesis), University of Cambridge, 1998.

[141] J.R.B. Knowling, Helium Atom Scattering: Experiment and the Interpretation of Experiment (Ph.D. thesis), University of Cambridge, 2000, URL https://www.repository.cam.ac.uk/handle/1810/251699.

[142] S. Dworski, Atom Optical Methods for Surface Studies (Ph.D. thesis), University of Cambridge, 2004, URL https://ethos.bl.uk/OrderDetails.do?uin=uk.bl.ethos.615678.

[143] M. DeKieviet, D. Dubbers, M. Klein, U. Pieles, C. Schmidt, Design and performance of a highly efficient mass spectrometer for molecular beams, Rev. Sci. Instrum. 71 (5) (2000) 2015–2018, http://dx.doi.org/10.1063/1.1150570.

[144] A.V. Kalinin, L.Y. Rusin, J.P. Toennies, Ion source with longitudinal ionization of a molecular beam by an electron beam in a magnetic field, Instrum. Exp. Tech. 49 (5) (2006) 709–713, http://dx.doi.org/10.1134/S0020441206050186.

[145] M. Bergin, D.J. Ward, S.M. Lambrick, N.A. von Jeinsen, B. Holst, J. Ellis, A. Jardine, W. Allison, Low-energy electron ionization mass spectrometer for efficient detection of low mass species, Rev. Sci. Instrum. 92 (7) (2021) 073305, http://dx.doi.org/10.1063/5.0050292.

[146] D.J. Riley, M. Mann, D.A. MacLaren, P.C. Dastoor, W. Allison, K.B. Teo, G.A. Amaratunga, W. Milne, Helium detection via field ionization from carbon nanotubes, Nano Lett. 3 (10) (2003) 1455–1458, http://dx.doi.org/10.1021/nl034460c.

[147] R.B. Doak, Y. Ekinci, B. Holst, J.P. Toennies, T. Al-Kassab, A. Heinrich, Field ionization detection of supersonic molecular beams, Rev. Sci. Instrum. 75 (2) (2004) 405–414, http://dx.doi.org/10.1063/1.1642743.

[148] R.B. Doak, The assessment of field ionization detectors for molecular beam use, J. Phys.: Condens. Matter 16 (2004) S2863–S2878, http://dx.doi.org/10.1088/0953-8984/16/29/002.

[149] J. Piskur, L. Borg, A. Stupnik, M. Leisch, W.E. Ernst, B. Holst, Field ionization of free helium atoms: Correlation between the kinetic energy of ionized atoms and probability of their field ionization, Appl. Surf. Sci. 254 (2008) 4365–4369, http://dx.doi.org/10.1016/j.apsusc.2008.01.053.

[150] D.P. DePonte, G.S. Elliott, S.D. Kevan, Current–voltage relation for a field ionizing He beam detector, J. Appl. Phys. 77 (4) (2009) 044910, http://dx.doi.org/10.1063/1.3081641.

[151] K.M. O'Donnell, A. Fahy, M. Barr, W. Allison, P.C. Dastoor, Field ionization detection of helium using a planar array of carbon nanotubes, Phys. Rev. B 85 (11) (2012) 113404, http://dx.doi.org/10.1103/PhysRevB.85.113404.

[152] C. Van de Runstraat, R.W. Van Resandt, J. Los, An absolute bolometer detector for energetic neutral particles, J. Phys. E Sci. Instrum. 3 (7) (1970) 575–578, http://dx.doi.org/10.1088/0022-3735/3/7/434.

[153] G.S. Hurst, M.G. Payne, M.H. Nayfeh, J.P. Judish, E.B. Wagner, Saturated two-photon resonance ionization of He (2 ^{1}S), Phys. Rev. Lett. 35 (2) (1975) 82–85, http://dx.doi.org/10.1103/PhysRevLett.35.82.

[154] S.L. Chin, Multiphoton Ionization of Atoms, Elsevier, 2012.

[155] D.A. Maclaren, Development of a Single Crystal Mirror for Scanning Helium Microscopy (Ph.D. thesis), University of Cambridge, 2002, https://www.repository.cam.ac.uk/handle/1810/251834.

[156] C.G. Herbert, R.A. Johnstone, Mass Spectrometry Basics, CRC Press, 2002.

[157] D.J. Douglas, Linear quadrupoles in mass spectrometry, Mass Spectrom. Rev. 28 (6) (2009) 937–960, http://dx.doi.org/10.1002/mas.20249.

[158] M. Szilagyi, Electron and Ion Optics, Springer Science & Business Media, 2012.

[159] H. Tuithof, A.H. Boerboom, H. Meuzelaar, Simultaneous detection of a mass spectrum using a channeltron electron multiplier array, Int. J. Mass Spectrom. Ion Phys. 17 (3) (1975) 299–307, http://dx.doi.org/10.1016/0020-7381(75)87040-9.

[160] T.A. Myles, A. Fahy, J. Martens, P.C. Dastoor, M.G. Barr, Fast neutral atom microscopy: An optimisation framework for stagnation detectors, Measurement 151 (2020) 107263, http://dx.doi.org/10.1016/j.measurement.2019.107263.

[161] M. Hillenkamp, S. Keinan, U. Even, Condensation limited cooling in supersonic expansions, J. Chem. Phys. 118 (19) (2003) 8699–8705, http://dx.doi.org/10.1063/1.1568331.

[162] T.A. Myles, S.D. Eder, M.G. Barr, A. Fahy, J. Martens, P.C. Dastoor, Taxonomy through the lens of neutral helium microscopy, Sci. Rep. 9 (1) (2019) 1–10, http://dx.doi.org/10.1038/s41598-018-36373-5.

[163] M. Bergin, T.A. Myles, A. Radic, C.J. Hatchwell, S.M. Lambrick, D.J. Ward, S.D. Eder, A. Fahy, M. Barr, P.C. Dastoor, Complex optical elements for scanning helium microscopy through 3D printing, J. Phys. D: Appl. Phys. 55 (2021) 095305, http://dx.doi.org/10.1088/1361-6463/ac3a3e.

[164] P.J. Witham, E. Sanchez, Simplified neutral atom microscopy, in: 2011 11th IEEE International Conference on Nanotechnology, 2011, pp. 535–540, http://dx.doi.org/10.1109/NANO.2011.6144498.

[165] A. Fahy, M. Barr, J. Martens, P. Dastoor, A highly contrasting scanning helium microscope, Rev. Sci. Instrum. 86 (2) (2015) 023704, http://dx.doi.org/10.1063/1.4907539.

[166] M. Barr, A. Fahy, J. Martens, A.P. Jardine, D.J. Ward, J. Ellis, W. Allison, P.C. Dastoor, Unlocking new contrast in a scanning helium microscope, Nature Commun. 7 (2015) 10189, http://dx.doi.org/10.1038/ncomms10189.

[167] B. Holst, Atom Optics and Surface Growth Studies using Helium Atom Scattering (Ph.D. thesis), University of Cambridge, 1997, URL https://ethos.bl.uk/OrderDetails.do?uin=uk.bl.ethos.604194.

[168] R. Bacon, Aspects of Atom Beam Microscopy and Scattering from Surfaces (Ph.D. thesis), University of Cambridge, 2007, URL https://ethos.bl.uk/OrderDetails.do?uin=uk.bl.ethos.596236.

[169] A.E. Weeks, Si(111) Atom-Optical Mirrors for Scanning Helium Microscopy (Ph.D. thesis), University of Cambridge, 2008, URL https://ethos.bl.uk/OrderDetails.do?uin=uk.bl.ethos.611911.

[170] K. O'Donnell, Field Ionization Detection for Atom Microscopy (Ph.D. thesis), University of Newcastle, 2009, URL https://ogma.newcastle.edu.au/vital/access/manager/Repository/uon:6255.

[171] D.M. Chisnall, High Sensitivity Detector for Helium Atom Scattering (Ph.D. thesis), University of Cambridge, 2013, URL https://ethos.bl.uk/OrderDetails.do?uin=uk.bl.ethos.607777.

[172] M.G. Barr, Imaging with Atoms: Aspects of Scanning Helium Microscopy (Ph.D. thesis), University of Newcastle, 2015, URL https://nova.newcastle.edu.au/vital/access/manager/Repository/uon:22446.

[173] G. Anemone, Development of Graphene Atomic Mirrors for Neutral Helium Microscopy (Ph.D. thesis), Universidad Autónoma de Madrid, 2017, URL https://repositorio.uam.es/h{and}le/10486/681667.

[174] R. Flatabø, Charged Particle Lithography for the Fabrication of Nanostructured Optical Elements (Ph.D. thesis), University of Bergen, 2018, URL https://Bora.Uib.No/Bora-Xmlui/H{and}Le/1956/23609.

[175] J. Martens, Prototype Permanent Magnet Solenoidal Ioniser for the Newcastle Scanning Helium Microscope (Ph.D. thesis), University of Newcastle, 2019, URL https://nova.newcastle.edu.au/vital/access/manager/Repository/uon:37871.

[176] A.S. Palau, On the Design of Neutral Scanning Helium Atom Microscopes (SHeM) - Optimal Configurations and Evaluation of Experimental Findings (Ph.D. thesis), University of Bergen, 2021, URL https://bora.uib.no/bora-xmlui/handle/11250/3009651.